

**MECHANISM AND EXPERIMENTAL VALIDATION OF INNOVATIVE SELF-  
CENTERING CONICAL FRICTION DAMPER**

by

Hengchao Xu

B.A., Central South University, 2017

A THESIS SUBMITTED IN PARTIAL FULFILLMENT OF  
THE REQUIREMENTS FOR THE DEGREE OF

MASTER OF APPLIED SCIENCE

in

THE FACULTY OF GRADUATE AND POSTDOCTORAL STUDIES

(Civil Engineering)

THE UNIVERSITY OF BRITISH COLUMBIA

(Vancouver)

December 2019

© Hengchao Xu, 2019

The following individuals certify that they have read, and recommend to the Faculty of Graduate and Postdoctoral Studies for acceptance, the thesis entitled:

Mechanism and experimental validation of innovative self-centering conical friction damper

submitted by Hengchao Xu in partial fulfillment of the requirements for

the degree of Master of Applied Science

in Civil Engineering

**Examining Committee:**

T.Y. Yang, Department of Civil Engineering, University of British Columbia, Canada  
Supervisor

Yao Cui, Department of Civil Engineering, Dalian University of Technology, China  
Additional Examiner

## **Abstract**

Past earthquakes have shown that traditional structural design relies on the component ductility to dissipate the earthquake energy. This has led to significant damage for the structure. Innovative energy dissipation devices have been developed in the past to dissipate the earthquake energy. However, the big disadvantage of energy dissipation devices is the lack of self-centering feature. Significant residual deformation can have effects on the building resilience. Failing to eliminate the residual deformation can lead to prolong downtime and significant financial losses. In this thesis, a novel damper named self-centering conical friction damper (SCFD) is proposed. SCFD utilizes conical, flat surfaces and post-tensioning tendons to resist the earthquake loads in all directions. The conical surfaces force the SCFD to self-center, making the SCFD highly desired for earthquake applications. In this thesis, detailed mechanical behavior for the SCFD was derived using theoretical equations in this thesis. The hysteresis behavior was verified through the experimental tests. The behavior observed from the test matches well with the theoretical solution. Using the derived equations, detailed parameter study including the influences of pretension forces, effective stiffness of post tension tendons, slope angle and friction coefficients have been investigated. Results show the hysteresis behavior can be achieved using different combinations of the slope angle, PT tendons and friction coefficients. Overall, high slope and friction coefficients will lead to highly efficient SCFD with lower demands on the PT tendons. Detailed design approaches have been presented which allows the engineers to design SCDF for different applications. Overall, this thesis shows the SCFD can be used efficiently for application in earthquake engineering with stable energy dissipation and self-centering capabilities.

## **Lay Summary**

Earthquakes cause a lot of damage which causes significant financial and casualty losses. In this thesis, a novel structural device, named self-centering friction damper (SCFD) is proposed. The SCFD can dissipate the earthquake energy and self center. This allows the building to be protected from earthquakes and be recovered shortly after the earthquake. Detailed analytical and experimental studies were conducted.

## **Preface**

This thesis is submitted as a completion requirement for the Master of Applied Science Degree in Civil Engineering degree at the University of British Columbia. The initial idea for this research was proposed by Professor T.Y. Yang , the author and PhD candidate Lisa Tobber. The author of this thesis was responsible for the literature review, mechanism development, experimental test, numerical simulation, data processing, results, and conclusion. The thesis was drafted by the author and revised based on comments from Professor T.Y. Yang. Part of this thesis will be rewritten as a peer-reviewed journal paper following the thesis publication.

# Table of Contents

<b>Abstract.....</b>	<b>iii</b>
<b>Lay Summary .....</b>	<b>iv</b>
<b>Preface.....</b>	<b>v</b>
<b>Table of Contents .....</b>	<b>vi</b>
<b>List of Tables .....</b>	<b>ix</b>
<b>List of Figures.....</b>	<b>x</b>
<b>List of Symbols .....</b>	<b>xiii</b>
<b>List of Abbreviations .....</b>	<b>xv</b>
<b>Acknowledgements .....</b>	<b>xvi</b>
<b>Dedication .....</b>	<b>xvii</b>
<b>Chapter 1: Introduction .....</b>	<b>1</b>
1.1    Background.....	1
1.2    Review of Conventional Passive Control Dampers.....	2
1.2.1    Metallic Dampers.....	2
1.2.2    Viscous Dampers .....	5
1.2.3    Viscoelastic Dampers.....	6
1.2.4    Conventional Friction Devices .....	7
1.3    Review of Self-centering Friction Device .....	11
1.4    Review of Proposed Self-centering System.....	14
1.5    Innovative Self-centering Conical Friction Damper (SCFD).....	15
1.6    Scope of Work .....	17

1.7	Organization of Thesis .....	18
<b>Chapter 2: Development of SCFD and Design Methodology .....</b>		<b>19</b>
2.1	Hysterical Behavior of SCFD .....	19
2.1.1	Determine Key Design Parameters .....	21
2.2	Design Criteria for SCFD .....	25
2.3	Equation Verification through Finite Element Model in Abaqus .....	27
2.3.1	Overview of Finite Element Model .....	27
2.3.2	Motion Observation & Equation Verification .....	31
2.4	Summary .....	32
<b>Chapter 3: Component Experiment of SCFD .....</b>		<b>33</b>
3.1	Test Setup .....	33
3.2	Specimen and Testing Matrix .....	34
3.3	Instrumentation .....	39
3.3.1	Load Feedback .....	39
3.3.2	Displacement Feedback .....	39
3.3.3	Pretension Force Feedback .....	41
3.4	Controller and Loading Protocol .....	41
3.5	Summary .....	42
<b>Chapter 4: Experiment Results and Parameter Study .....</b>		<b>43</b>
4.1	Experimental Results .....	43
4.1.1	Overview of Test Results .....	43
4.1.2	Summary of Experimental Results and Verifications of Equations .....	44
4.1.3	Discussion on Energy Dissipation .....	46

4.2	Parameter Study .....	48
4.3	Optimal Design Approach .....	50
4.4	Summary .....	52
<b>Chapter 5: Summary and Conclusions .....</b>		<b>53</b>
5.1	Conclusion .....	53
5.2	Future work .....	54
<b>Bibliography .....</b>		<b>55</b>
<b>Appendices.....</b>		<b>59</b>
	Appendix A.....	59
	Appendix B.....	64
	Appendix C.....	66
	Appendix D.....	70
	Appendix E.....	72

## List of Tables

Table 3.1 Design Parameters .....	35
Table 3.2 Testing Matrix.....	38

## List of Figures

Figure 1.1 ADAS damper .....	2
Figure 1.2 Typical hysteresis of ADAS damper .....	2
Figure 1.3 Steel slit damper and its hysteresis .....	3
Figure 1.4 Honeycomb damper .....	3
Figure 1.5 Welded Wide Flange Fuse .....	4
Figure 1.6 Honeycomb structural fuse .....	5
Figure 1.7 Typical viscous damper .....	6
Figure 1.8 Viscoelastic fused coupling beam .....	6
Figure 1.9 Friction damped braced frame .....	7
Figure 1.10 Slotted bolted connection .....	8
Figure 1.11 Braced frame having slotted bolted connection .....	8
Figure 1.12 Components of a novel friction device .....	9
Figure 1.13 Motion of the novel friction device .....	10
Figure 1.14 Testing of a modified rotational friction damper .....	10
Figure 1.15 Energy dissipating restraint .....	11
Figure 1.16 Flag shape and double-triangular shape hysteresis and hysteresis .....	12
Figure 1.17 Friction based ring spring damper .....	13
Figure 1.18 Resilient slip friction joint (a) Cap plates and slotted plates (b) Belleville washers (c) High strength bolts (d) Assembled joint .....	13
Figure 1.19 Two examples of self-centering system .....	14
Figure 1.20 SCFD concept.....	16
Figure 1.21 SCFD having all-direction motion .....	16

Figure 2.1 Exploded view of SCFD.....	17
Figure 2.2 Damper motion and the corresponding hysterical behavior.....	20
Figure 2.3 Clamping plate A opens as the inner plate moves.....	21
Figure 2.4 Free body diagram as the inner plate moves to the right.....	22
Figure 2.5 Free body diagram as the inner plate moves to the left.....	23
Figure 2.6 Three different types of hysteresis (a) Type I (b) Type II (c) Type III .....	25
Figure 2.7 Belleville washer mechanism (a) No deformation (b) Under compression .....	26
Figure 2.8 Pair of cones modeled in Abaqus : (a) Female cone - rigid element (b) Male cone - finite element .....	27
Figure 2.9 Clamping plate A.....	28
Figure 2.10 Clamping plate B.....	28
Figure 2.11 Assemble view in Abaqus .....	29
Figure 2.12 Three different contact surfaces: (a) Conical contact surface (b) Flat contact surface (c) Stopper-Clamping plate contact surface.....	30
Figure 2.13 Summary of boundary conditions .....	31
Figure 2.14 Motion examples (a) Max to the right (b) max to the left.....	32
Figure 2.15 Comparison between theory and simulation .....	32
Figure 3.1 Test setup and the specimen installed (a) Set up (b) Back&top view of the specime.	34
Figure 3.2 Clamping plate A with female cone .....	35
Figure 3.3 End plate and clamping plate B.....	36
Figure 3.4 Steel plate with male cone.....	37
Figure 3.5 (a) High strength bolts (b) Belleville washers.....	37
Figure 3.6 Actuator and load cell.....	39

Figure 3.7 (a) Concept of getting displacement feedback (b) Linear pots configuration .....	40
Figure 3.8 Condition box and bolt in tensile test .....	41
Figure 3.9 ACTS controller .....	42
Figure 3.10 Loading protocol .....	42
Figure 4.1 Experimental results .....	45
Figure 4.2 Sensitivity check on (a) sliding force (b) post stiffness .....	46
Figure 4.3 Cumulative energy dissipation of different specimens over the test .....	47
Figure 4.4 Energy dissipation plot against the pretension force and the number of washers .....	48
Figure 4.5 Normalized sliding force .....	49
Figure 4.6 Normalized post stiffness .....	50
Figure 4.7 Normalized unloading stiffness .....	50
Figure 4.8 Flow chart of recommended design approach .....	51

## List of Symbols

$A$  : Area of truss wire.

$E$  : Elastic modulus of truss wire material.

$F$  : Force in truss wire.

$F_f$  : The friction force generated between the friction pad and the steel plate

$F_f'$  : The friction force generated along the conical surface

$F_{pt}$  : The normal force in the high strength bolt.

$F_{pt}^0$  : The initial pretension force applied to the bolts.

$K$  : The axial stiffness of truss wire.

$k_{pt}$  : The effective stiffness of post tension tendons

$k_p$  : The post stiffness.

$k_u$  : The unloading stiffness

$k_{ws}$  : The individual washer stiffness

$n_p$  : The number of washers stacked in parallel.

$n_s$  : The number of washers stacked in series.

$L$  : The length of the truss wire.

$P$  : External applied force to the damper

$P_{capacity}$  : Force capacity of stacked washers.

$P_{demand}$  : Force demand for stacked washers.

$P_m$  : The maximum force.

$P_r$  : The residual force.

$P_s$  : The system slipping force

$P_u$  : The unloading force.

$P_{ws}$  : Force capacity of individual washer

$\alpha$  : The thermal expansion coefficient.

$\Delta_m$  : The maximum deformation happening to the damper.

$\Delta T$  : Change of temperature.

$\delta_{capacity}$  : Deformation capacity of stacked washers.

$\delta_{demand}$  : Deformation demand for stacked washers.

$\delta_{ws}$  : Deformation capacity of individual washer.

$\mu$  : The friction coefficient between the friction pad and the steel plate.

$\mu_{critical}$  : The corresponding critical friction coefficient between the friction pad and the steel plate.

$\mu'$  : The friction coefficient between conical surfaces.

$\theta$  : The cone slope angle

$\theta_{critical}$  : The critical slope angle

## List of Abbreviations

DOFs: Degree of freedoms

HSF: Honeycomb structural fuse

LP: Linear pot

PFDC: Post-tensioned friction damped connection

PID: Proportional–integral–derivative

PT: Pretension

PTFD: PT beam-to-column connection with friction damper

RSFJ: Resilient slip friction joints

SCFD: Self-centering conical friction damper

SG: Strain gauge

SSD: Steel slip damper

WWFF : Welded Wide Flange Fuse

## **Acknowledgements**

I would like to sincerely thank my supervisor Prof. T.Y. Yang. It was such an honor and pleasure for me to be his student and do research with Smart Structure Research Group. Being a supervisor, Prof. T.Y. Yang is always showing great support to my work. His passion on pursuing new technology to earthquake engineering and his patience on advising me have always motivated me to move forward. It was such a wonderful experience to do brainstorm together, come up with new ideas, work out all the details and find smart ways to solve problems with him.

Furthermore, I would like to thank Dorian Tung for helping me solve experimental issues and revising fabrication drawings. Sincere thanks to my research colleague Lisa Tobber, who has been always kindly giving me guidance and helping me with my research. I am very grateful to have such an amazing colleague and really enjoy the time working together to find solutions for either design or research issues. I've learned a lot from her. I would also like to extend my thanks to other research colleagues who have been giving valuable input to my research: Fabrício Bagatini-Cachuço, Hongzhou Zhang, Sirou Zhuo, Yuxin Pan, Xu Xie, Hamidreza Etebarian and Mohammad Amin Sadeghi. Also, I would like to thank Doug Hudniuk, Scott Jackson, Sylvain Picard, Simon Lee and Harald Schremp for their help to make the experiment happen. My friends, Tianyi Li, Doudou Tan, Xiao Pan thank you all for the friendship. I really appreciate it.

Most of all, I would like to express my gratitude for my parents' unconditional love and support. I would never make such achievements without them.

## **Dedication**

*To my parents for their unconditional love and support*

.

# Chapter 1: Introduction

## 1.1 Background

Earthquakes have been causing significant losses to both economy and human life. Engineers have been working hard on ensuring the building behaves well when the earthquake comes. However, the traditional design approach mainly takes advantages of stiffness, strength and ductility of essential structural components including beams and columns. Such approach can only ensure that the building won't collapse during the earthquake. But most of the building needs to be wiped out due to their intensive damage. Even the buildings having serious residual deformation requires demolition. Thus, the down time is significantly prolonged. To achieve instant occupancy after the earthquake shock, structural fuses are getting more and more popular in earthquake design. Structural fuses are normally designed to yield first, thus protecting the main structural components from getting any further damage. Especially, passive control dampers are one of the most practical ways to reduce the dynamic response of the building subjected to earthquake loads. Many different types of passive dampers have been previously investigated (Amjadian et al. 2017; Gong et al. 2017; Mahjoubi et al. 2015; Soong et al. 2002; Symans et al., 2008). Literature reviews are presented on conventional passive control dampers such as metallic dampers, viscous dampers, viscoelastic dampers and conventional friction device. In addition, self-centering friction devices and self-centering friction damped systems are also reviewed.



several steel plates in parallel. However, it is loaded in strong axis direction, the stiffness can be significantly increased (Figure 1.2). By changing the length and width of individual plate, the resultant stiffness can be very different. It is clear seen that longer or wider plate has less stiffness than that of shorter or narrower one. This is because shorter or narrower ones have shear controlled yielding mechanism. Flexural yielding mechanism mostly relies on the material at both ends of the plate, it is a waste of material to have even width along the clear span. It is smarter to use the honeycomb damper proposed by Kobori et al. (1992) because the honeycomb shaped plate has more evenly distributed yielding. Thus, the material can be fully used. In further study, Ma et al. (2010) conducted more experimental tests and investigated how the geometry dimension will make differences to the hysteresis of honeycomb damper.

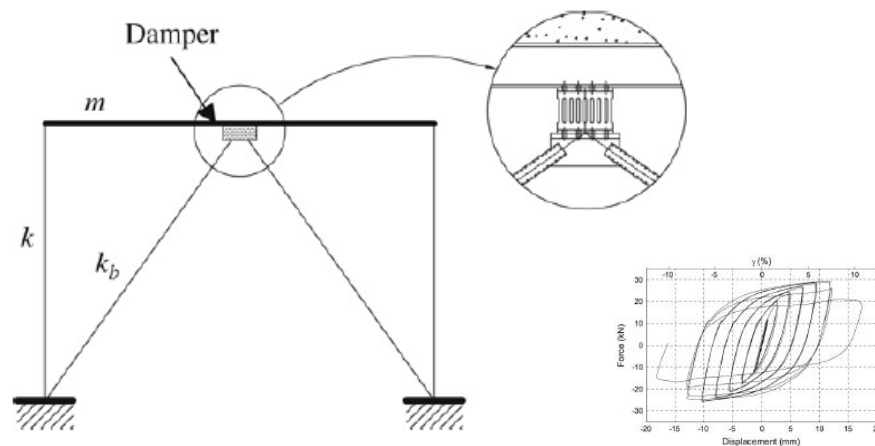


**Figure 1.3 Steel slit damper and its hysteresis (Chan et al. 2008)**

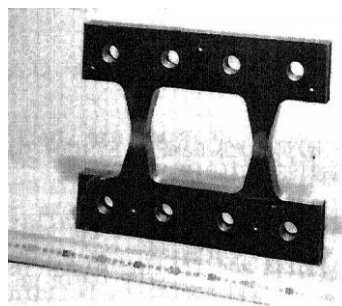


**Figure 1.4 Honeycomb damper (Kobori et al., 1992)**

All these dampers require precise fabrication and lead to high cost. In order to minimize the fabrication cost, a new type of metallic damper named the Welded Wide Flange Fuse (WWFF) was proposed by Banjuradja (2018). Commonly available welded wide flange section is utilized. Holes will be drilled on the flanges such that WWFF can be easily bolted to the structure. In the study, different plate aspect ratios (defined as web width to web depth) and plate slenderness (defined as web depth to web thickness) were investigated in a set of experimental tests. As slenderness increases, the hysteresis shows higher stiffness, higher peak force and more pinching behavior. Smaller slenderness can provide more stable hysteresis. In addition, plate buckling and yielding through the tension field action occurred, moving the fracture to the center of the web. It is also found that the aspect ratio barely changes the hysteresis shape. But as the aspect ratio increases, the buckling shape changes from two parallel lines in the loading direction to diagonal buckling shape.

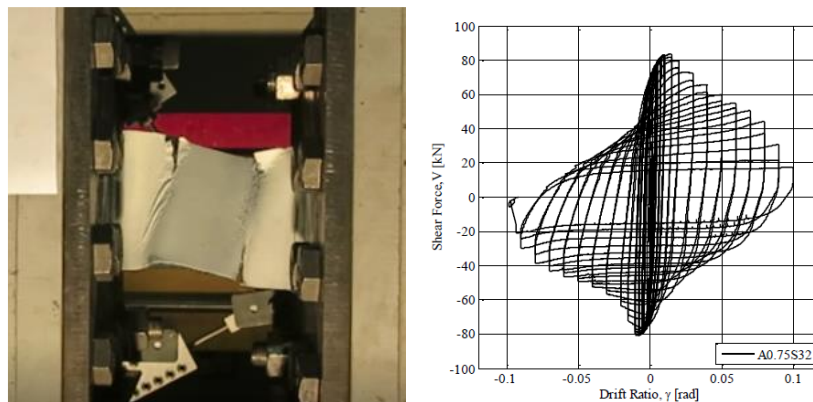


**Figure 1.5 Welded Wide Flange Fuse (Banjuradja, 2018)**

WWFF doesn't show good ductility. In order to make the plate more ductile, Yang et al. (2019) proposed an innovative honeycomb structural fuse (HSF). Many of honeycomb shaped holes were added to the WWFF. Figure 1.6 shows that HSF has various row-column cell patterns. By introducing more geometry parameters, users have more freedom to customize the stiffness,

ductility and force capacity. The experimental tests show that as cell aspect ratio increases, failure modes switch from local bending failure to global shear failure. At the same time, it is found that more rows can bring lower aspect ratio while more columns can bring higher aspect ratio. In addition, when the aspect ratio is low, fractures occur at ends of the cells; when the aspect ratio is high, fracture occurs in a diagonal pattern across the entire plate.

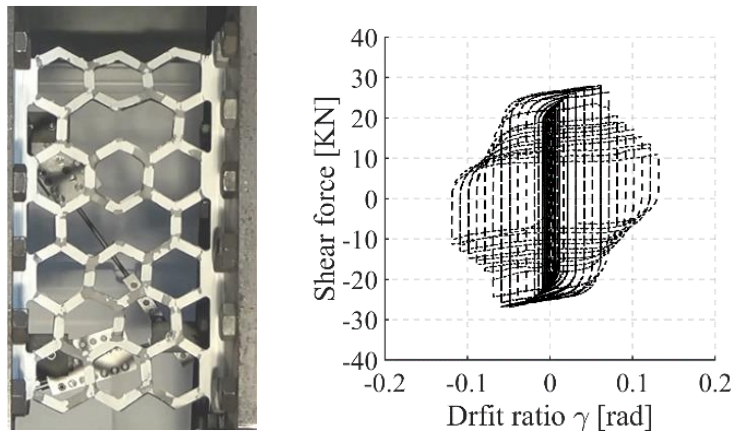


**Figure 1.6 Honeycomb structural fuse (Li, 2018)**

### 1.2.2 Viscous Dampers

Viscous damper normally adopts a tube as its body and such hollow cylinder is typically filled with certain fluid. (Figure 1.7) As the motion happens, the piston head starts pushing and pulling the fluid inside the tube. At the same time, the resulting difference in pressure across the piston head can lead to very large forces resisting the motion. It is concluded by Symans et al. (2008) that viscous damper has advantages of simplifying the damper modeling approach and behaving independently on frequency and temperature. However, there is also disadvantage of having possible fluid leaking.

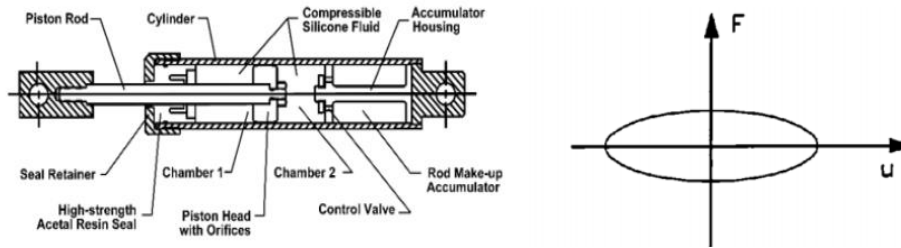


Figure 1.7 Typical viscous damper (Reinhorn, Li, & Constantinou, 1995)

### 1.2.3 Viscoelastic Dampers

Instead of using fluid, viscoelastic dampers mostly utilize the viscoelastic layer to achieve proper behavior. A typical viscoelastic damper installed in buildings usually consists of two viscoelastic layers sandwiched between metallic plates. Figure 1.2 shows a new viscoelastic fused coupling beam developed by Christopoulos et al. (2013). It clearly shows the difference in terms of hysteresis compared to viscous damper. Viscoelastic dampers are designed to have certain post stiffness while the viscous dampers usually have zero post stiffness during the motion. It is concluded by Symans et al. (2008) that viscoelastic damper has advantages of providing restoring forces due to its existing stiffness. There are also disadvantages including limited deformation capacity and dependency on loading frequency and environmental temperature.

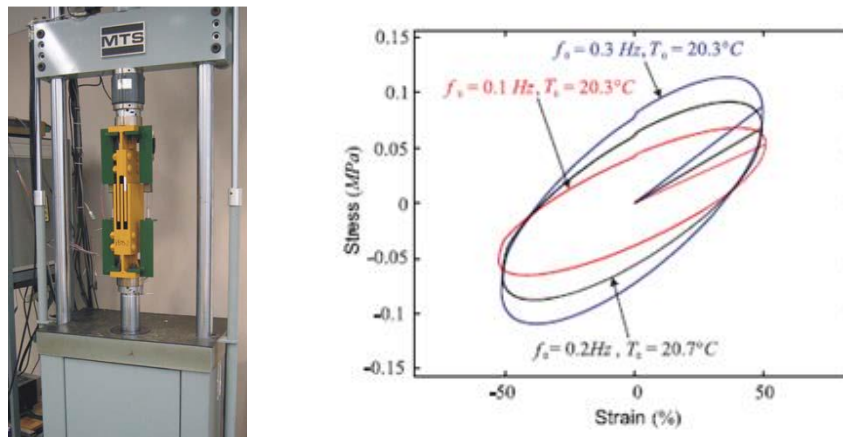


Figure 1.8 Viscoelastic fused coupling beam (Montgomery et al. 2015)

#### 1.2.4 Conventional Friction Devices

Friction damper is one of the popular damper due to their high energy dissipation capacity and easy fabrication requirement. The typical mechanism of friction damper is to dissipate the earthquake energy through sliding friction between steel plates. In many instance, high strength tension bolts are used to create the normal pressure needed between the sliding surfaces. Pall et al. (1982) developed and tested a friction damped braced frame, which adopted the friction device with one frictional slip joint at the intersection of the two diagonal braces (Figure 1.9). The device is connected to the braces through four rotational joints. It is found in the test that braced frame having such device has significantly less roof drift, beam moments and base shear forces. Yielding members were observed in normal braced frame, while none of the members yield in the friction damped frame.



Figure 1.9 Friction damped braced frame (Pall et al. 1982)

Grigorian et al. (1993) proposed a slotted bolted connection energy dissipator (Figure 1.10). This is a very simple friction device, mainly working in axial direction and being installed in braced frame (Figure 1.11). The component experiment conducted by the author showed that friction generated between steel plates vary significantly over the whole hysteresis, while friction

occurring between steel plate and brass plate is more stable. By adopting the brass plate as main friction pad, the elastic-perfectly-plastic behavior can be achieved.

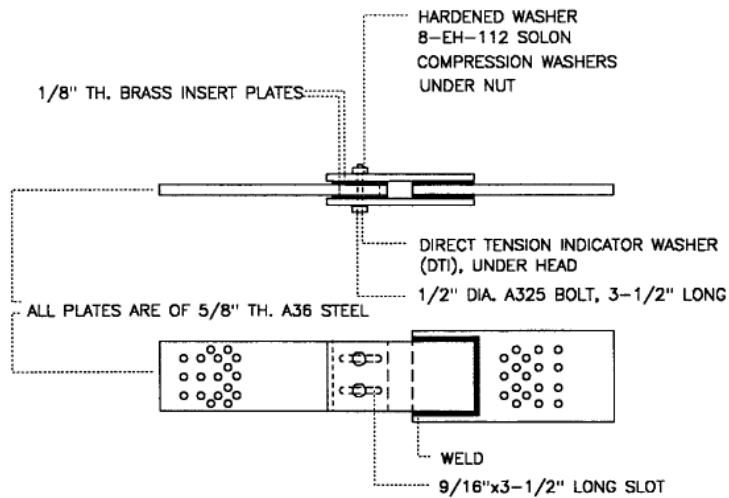


Figure 1.10 Slotted bolted connection (Grigorian et al., 1993)

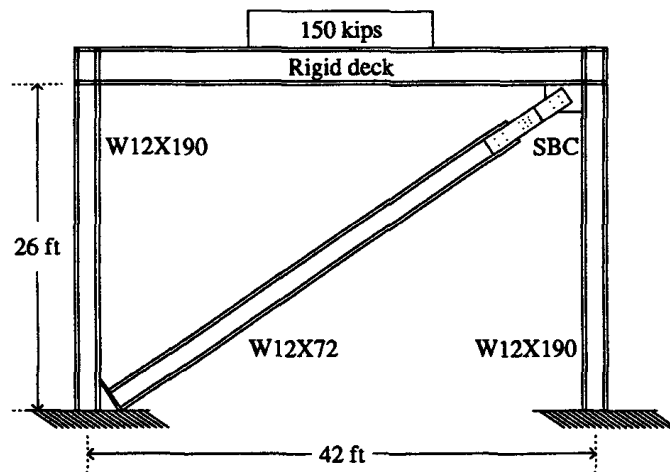
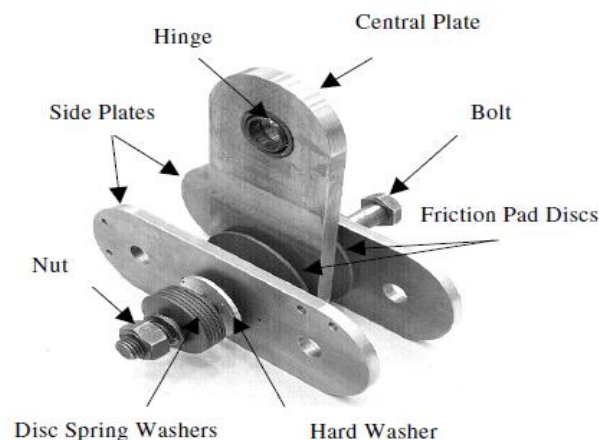


Figure 1.11 Braced frame having slotted bolted connection (Grigorian et al., 1993)

Mualla et al. (2002) proposed a novel friction damper dissipating energy through rotating instead of sliding, which was commonly found in conventional friction devices. As is shown in Figure 1.12, this novel friction damper consists of three steel plates: one central plate connected to the

frame through a hinge and two other side plates. In addition, two more friction pads are placed at both sides of the central plate. One high strength bolt goes through three plates and two friction pads along the center. After pretension force is applied to the bolt, the central plate and two friction pads are clamped by two side plates. In total, there are four main friction surfaces. Two more rods are used to connect two side plates through the holes at both sides so that they can behave as a full body. Then each rod is connected to the base of the brace (Figure 1.13). As the brace deforms, the central plate rotates against the frame and the side plates rotate against the central plate. Energy is dissipated through rotational friction occurring between friction pads and three plates. The advantage of using three pin connections is that not only more deformation capacity is provided but also more energy is dissipated. The use of disc spring washers prevents the pretension force from decreasing, thus brings a more stable hysteretic response. The author also investigated the influence of loading frequency has on the hysteresis. It is shown in test results that the excitation frequency makes no difference within a certain range.



**Figure 1.12 Components of a novel friction device (Mualla et al. 2002)**

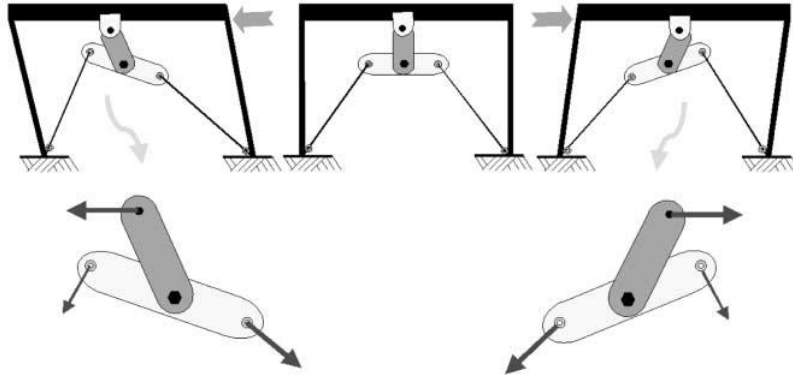


**Figure 1.13 Motion of the novel friction device (Mualla et al. 2002)**

This damper is later modified by Monir et al. (2013) to have five rotational friction hinges (Figure 1.14). The energy dissipation capacity is extremely increased. Theoretical equations were developed and verified by the experimental results. It is shown that the behavior can be well predicted and stable over the entire loading process. However, it is observed in the test that the hysteresis is asymmetrical due to its special geometry. A system level numerical study was also performed, showing that the modified friction damper can effectively reduce the dynamic response of the building subjected seismic load.



**Figure 1.14 Testing of a modified rotational friction damper (Monir et al. 2013)**

### 1.3 Review of Self-centering Friction Device

Though friction dampers have good capacity of energy dissipation, the residual deformation is hardly eliminated after the earthquake is gone, as is observed in all previous study, which can greatly increase the repair cost and time. Different self-centering mechanisms have been proposed by researchers to achieve zero residual deformation. One of the most popular way is to improve the friction damper itself. Richter et al. (1990) proposed and tested an energy dissipating restraint (Figure 1.15). Test results are summarized and presented by Aiken et al. (1993). In addition, parameter study is conducted by Nims et al. (1993). There are some principle components in this device: compression wedges, the spring inside the tube, stoppers and gaps at both sides of the spring. By adjusting the initial compression and tension gap to be zero, internal body can hit the stoppers right away and the spring starts being compressed, in which situation the device can always self-center since the spring restoring force is higher than friction resistance. This device can behave in two different types of self-centering hysteresis up to the initial force inside the spring. If the bolt is pretensioned, there is friction generated between the wedges. The applied force needs to reach the slip force first, which will give a flag-shape hysteresis (Figure 1.16). However, if no pretension force is applied, the slip force turns to zero, then the hysteresis changes to double-triangular shape (Figure 1.16).

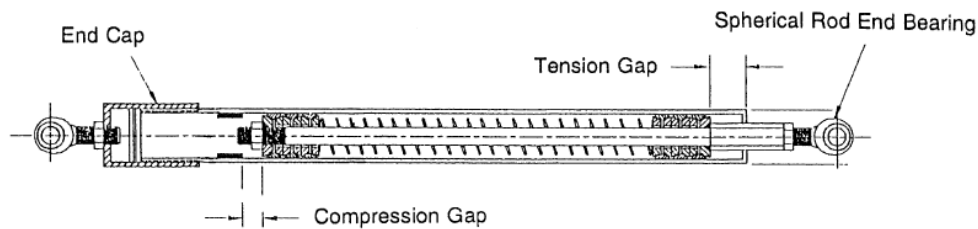
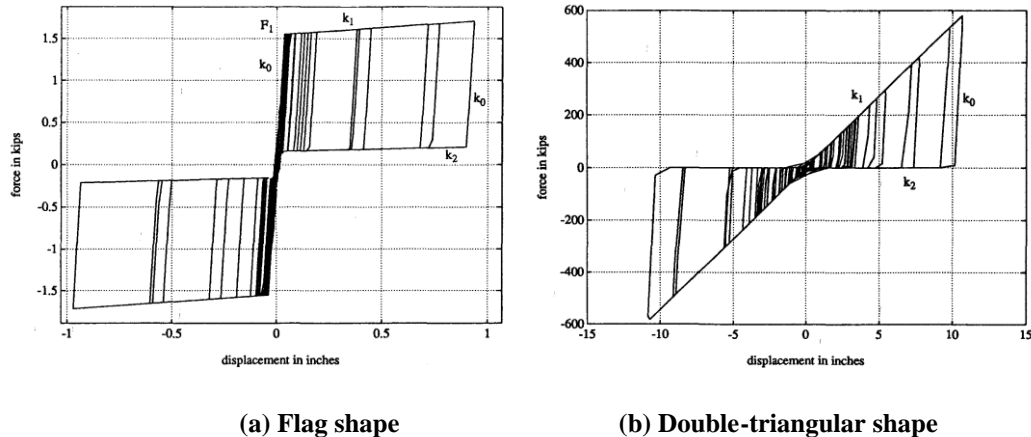
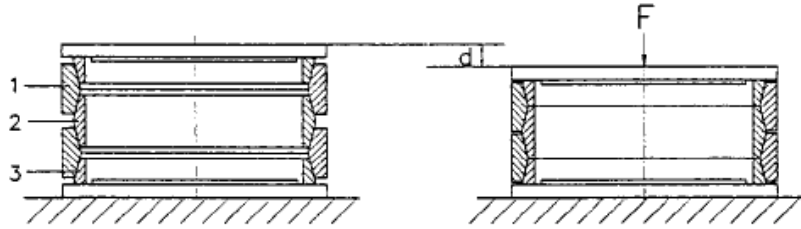


Figure 1.15 Energy dissipating restraint (Aiken et al., 1993)



**Figure 1.16 Flag shape and double-triangular shape hysteresis and hysteresis (Nims et al., 1993)**

Filiatrault et al. (2000) did numerical and experimental study on a novel friction-based ring spring damper, which can also effectively dissipate energy and self-center. Unlike the conventional friction damper, this novel one doesn't need pretension force from high strength bolts. As the damper is pulled in and out during an earthquake, inner rings move against outer rings (Figure 1.17), which brings normal pressure to the contact surfaces, thus friction is generated between them. The specially designed wedge slope can always bring zero residual deformation. Especially, frequency dependency test and durability test were carried out by the author. In general, all the characteristics are nearly independent on the excitation frequency. Though the loading stiffness showed correlation to the frequency, it is not representative due to unexpected errors during the test. It is also found in the durability test that the degradation of energy dissipation and peak forces is limited within 4%, showing that this damper can provide stable response under seismic loading. This innovative damper was also tested in a frame system subjected to 100% EI Centro and successfully brought the peak deformation down by almost 50%, the peak acceleration down by close to 30%. In addition, the damper has dissipated 20% of the input energy, protecting the frame from getting severe damage.



**Figure 1.17 Friction based ring spring damper (Filiatrault et al., 2000)**

By adapting the similar wedge design observed in the energy dissipating restraint (Richter et al. 1990) and the friction-based ring spring damper (Filiatrault et al. 2000), Hashemi et al. (2017) proposed an innovative resilient slip friction joint (RSFJ), which is applied to a timber rocking wall in their study. Two slotted plates in RSFJ are sandwiched by another two cap plates from top and bottom respectively (Figure 1.18). Bolts are pretensioned and provide normal pressure to the wedge surfaces. As the motion occurs, slotted plates in the middle move against the cap plates and push the one on the top up and the one on the bottom down. Belleville washers are used to compensate this additional deformation along the bolts and contribute to the post stiffness of the damper. The slope observed in RSFJ is as low as 15 degrees because special lubricant was applied to the friction surface so that friction coefficient is brought down.

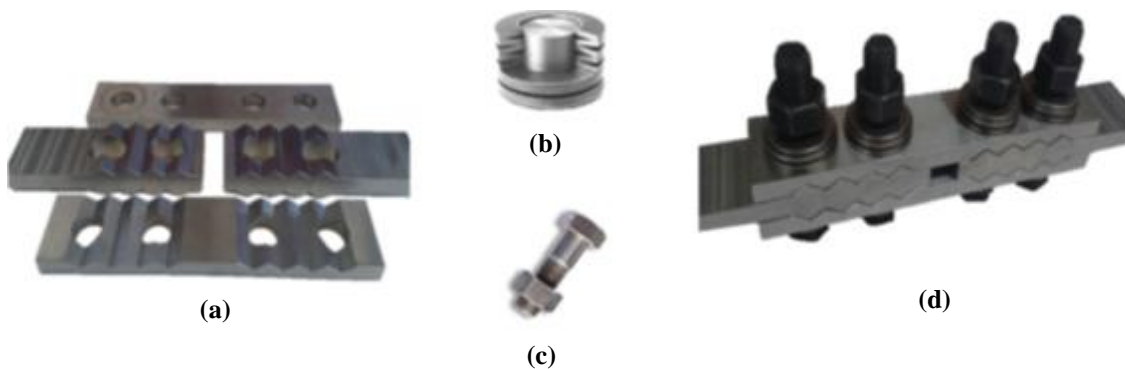


**Figure 1.18 Resilient slip friction joint (a) Cap plates and slotted plates (b) Belleville washers (c) High strength bolts (d) Assembled joint (Hashemi et al., 2017)**

## 1.4 Review of Proposed Self-centering System

Another way is to combine PT strands with conventional friction damper ( Rojas et al. 2005, Tsai et al. 2008). The typical way is to install conventional friction damper at both sides of the beam. They are either placed on both top and bottom flange or placed on the web. Then PT strands go parallel to the center line of the beam at both sides. As deformation occurs, relative rotation happens between beam and columns, energy is dissipated through sliding friction. At the same time, PT strands get stretched and has increasing internal force. Later the tension force of the PT strands can conquer the friction resistance and bring the beam back with no residual deformation left.

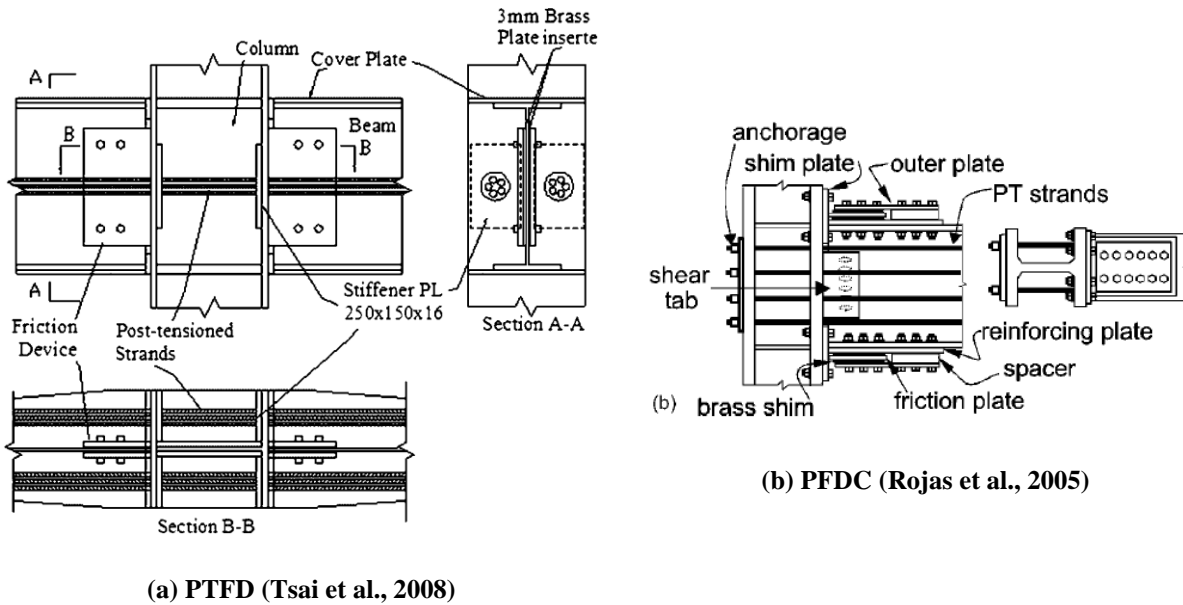
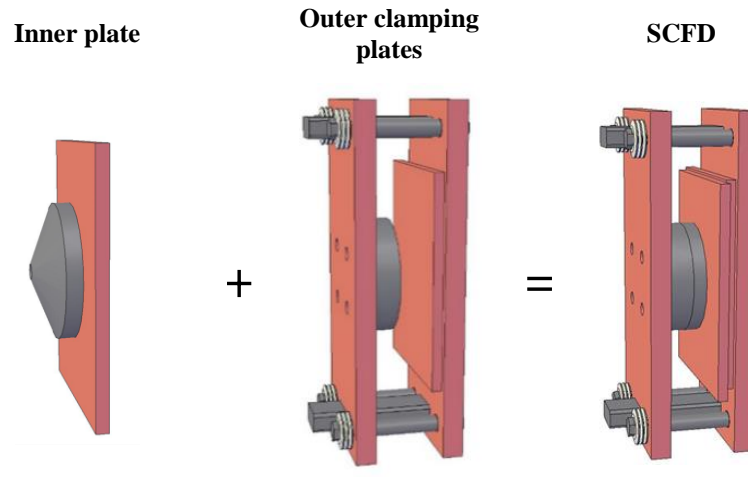


Figure 1.19 Two examples of self-centering system

## **1.5 Innovative Self-centering Conical Friction Damper (SCFD)**

In this study, an innovative self-centering conical friction damper (SCFD) which can resist loads in all directions (axial, shear and moment) is proposed. The detailed mechanism of the SCFD is presented. The behavior of the SCFD is verified using experimental tests. The result shows the proposed mechanical equations can well predict the response of SCFD. The developed mechanical equations are then used to optimize the design of the SCFD. Detailed optimized design charts are provided which designers can use to design different SCFD for different applications.

Figure 1.20 shows the mechanism of SCFD. A SCFD consists of an inner plate and outer clamping plates. The inner plate has a male cone surface on the front end and a flat surface the back end. The outer clamping plates has the female cone surface on one end and a flat surface at the other to sandwich the inner plate. Post-tensioning tendons are added to provide high compression forces between the inner and outer plates. The SCFD is designed to move in all in-plane directions, including vertical, horizontal and rotation movements. Figure 1.21 shows the relative movements of the inner plate with respect to the clamping outer plates. Because the inner and outer plates are confined by a male and female cone, as the inner plate move in the in-plane translational directions (horizontal or vertical movements), the normal force created by the PT tendons will force the inner and outer plates back to the original position. Hence, SCFD will always self center. As there are two sliding surfaces between the inner and outer plates, SCFD can be tuned to have different friction coefficients between these two sliding surfaces.



**Figure 1.20 SCFD concept**

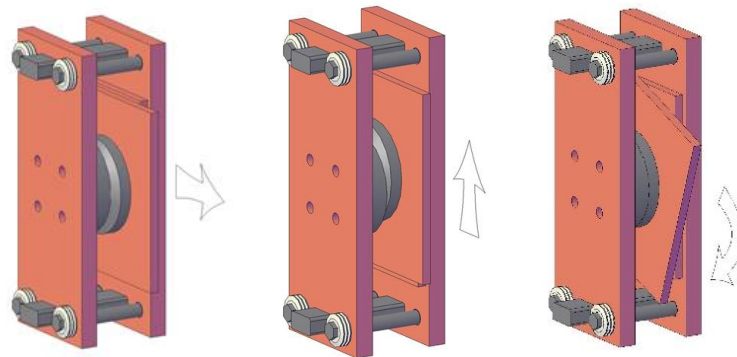


**Figure 1.21 SCFD having all-direction motion**

Figure 1.22 shows the assembly view of the SCFD. In short, SCFD consists of outer clamp plate A, outer clamp plate B and the inner plate. In the configurations presented, end plates are added at the end of clamp plate A and clamp plate B, which can be used to connect the structures. To prevent the relative in-plane rotational movement between the outer clamp plate A and outer clamp plate B, a stopper is added. The SCFD is connected using PT tendons.

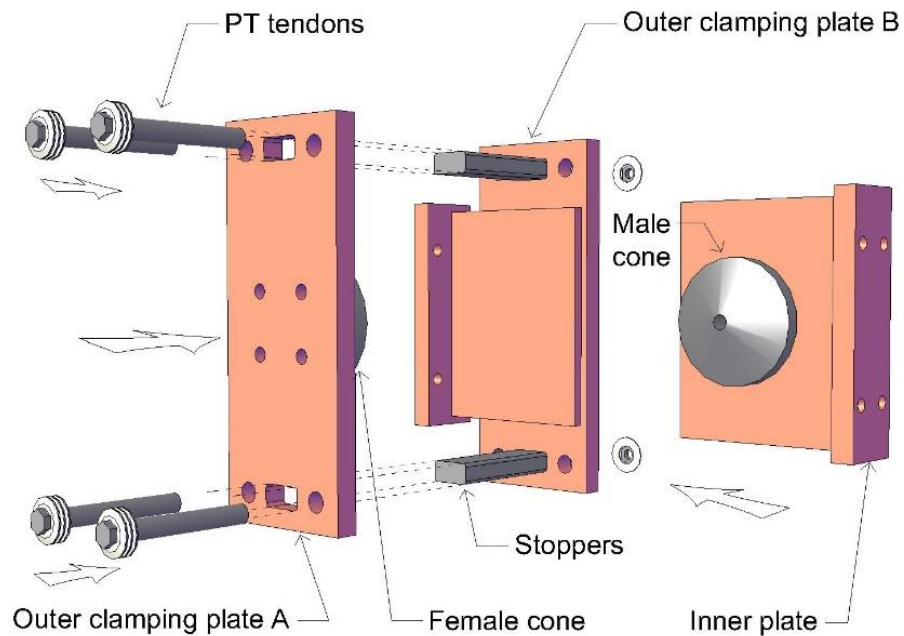


**Figure 1.22 Exploded view of SCFD**

## 1.6 Scope of Work

The research presented in this thesis has four main objectives:

- The first objective is to study the proposed self-centering mechanism and develop design equations for SCFD.
- The second objective is to conduct component experiment tests to validate the SCFD behavior.
- The third objective is to carry out more parameter study using the verified theoretical equations and propose design approaches which can be used by users to design SCFD for different applications.

## **1.7 Organization of Thesis**

Development, experiment and parameter study of SCFD was presented in the following five chapters:

Chapter 1 provides the background of this study. Previous studies were summarized in the literature review. Concept of SCFD was introduced in the end and its main components were described.

Chapter 2 proposes the desired hysteretic behavior of SCFD and gave a detailed discussion on each stage of the motion. Theoretical equations were also developed for all essential parameters. In addition, design methodology for post tension tendon and the self-centering feature was described.

Chapter 3 shows the prototype designed for the component experiment and its testing matrix. Test setup, instrumentation plan and loading protocol were summarized.

Chapter 4 presents the experimental results and the observation to the results was discussed. Prediction made by equations was compared against the experimental results. Design approach was developed for users who want to apply SCFD to building design.

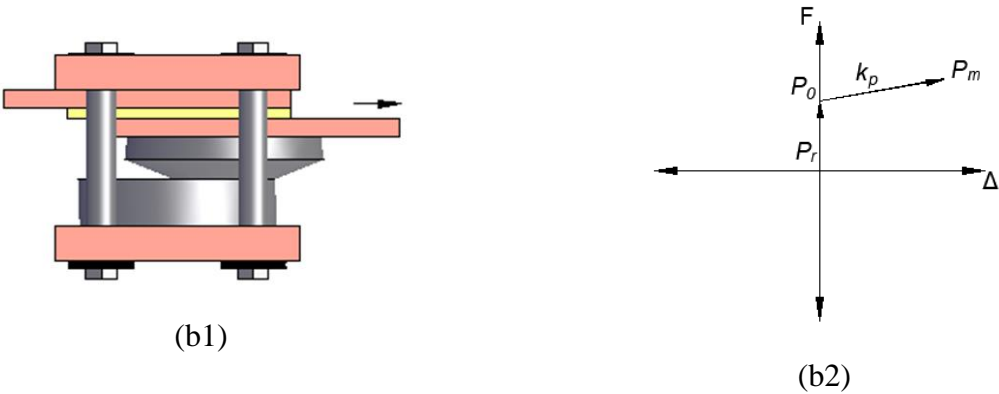
Chapter 5 summaries observations, conclusions from the study and topics for future research.

# Chapter 2: Development of SCFD and Design Methodology

Self-centering mechanism is very popular in either component level or system level. Many self-centering device and system have been proposed in recent years. This chapter first introduced the self-centering mechanism adopted in SCFD, then described its hysterical behavior in detail. Design equations for critical points shown in the proposed hysteresis were also developed in this chapter. Additionally, more information on how Belleville washers behave and are designed were presented. At the end of this chapter, design criteria for other parts of SCFD were discussed.

## 2.1 Hysterical Behavior of SCFD

The SCFD is designed to slide after the force exceed the initial sliding force,  $P_0$ . After that, the SCFD is designed to move with a post-yield stiffness,  $k_p$ . When the motion revered the direction, the SCFD is expected to drop in force to the unloading force  $P_u$ . The SCFD is designed to move back to the initial position with the unloading stiffness until it reaches zero displacement with the residual force,  $P_r$ . Figure 2.1 shows the hysteretic behavior of the SCFD. The result shows the SCFD can self-center with good energy dissipation.



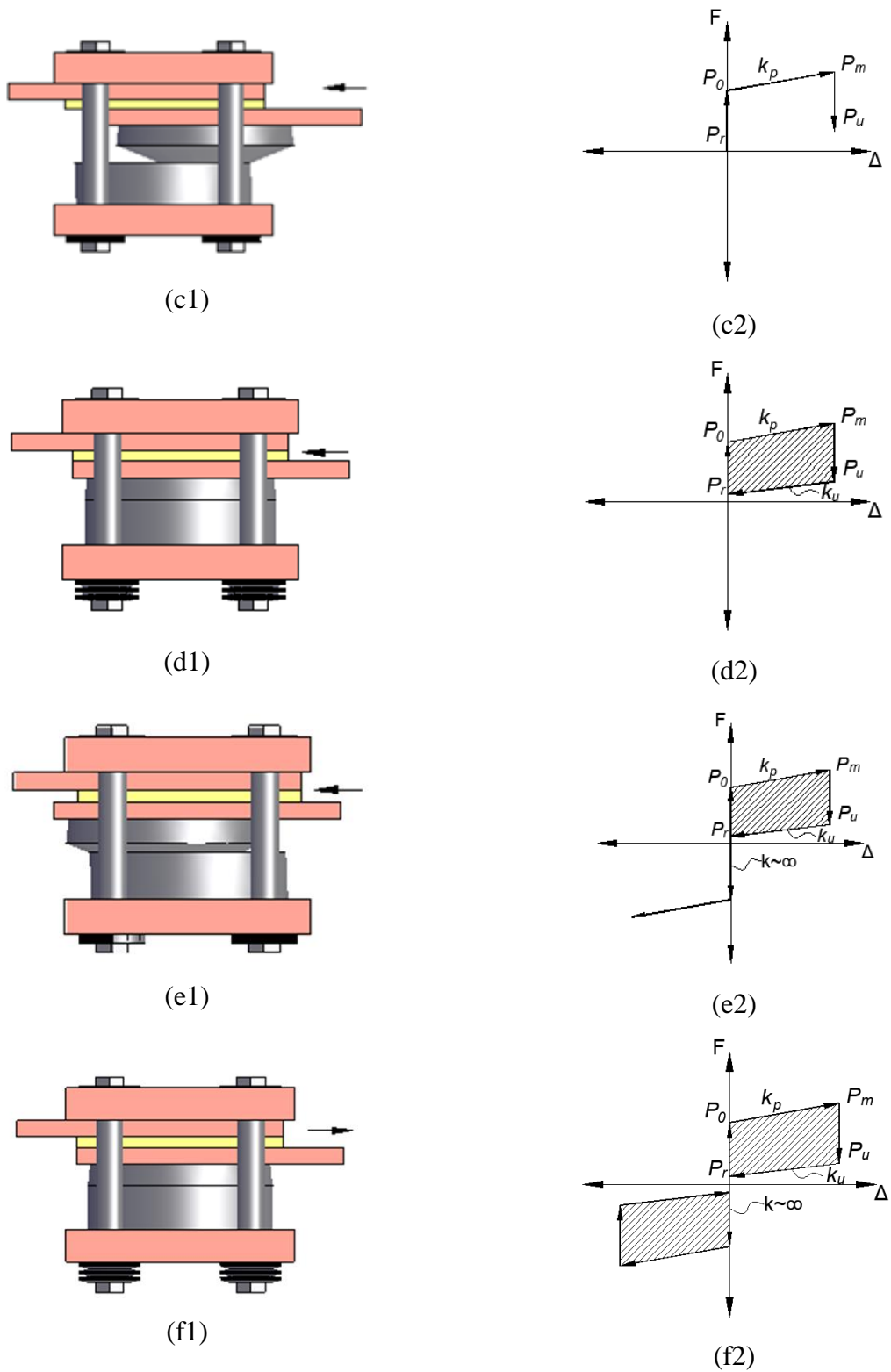


Figure 2.1 Damper motion and the corresponding hysterical behavior

### 2.1.1 Determine Key Design Parameters

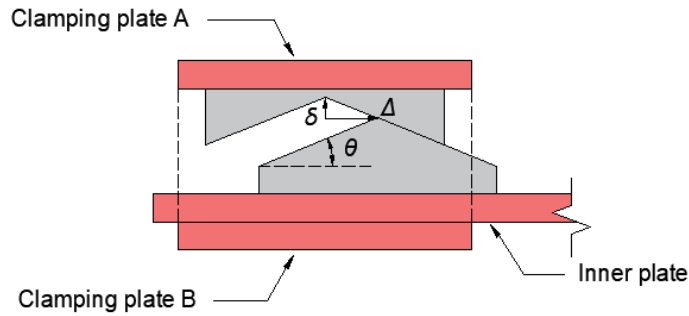
Figure 2.2 shows the geometry of the SCFD as the inner plate moves from left to right. Because of the cone shape configuration, when the inner plate is moved from left to the right with a distance  $\Delta$ , outer clamping plates will move up by a distance  $\delta$ . Equation 1 show the geometry transformation between  $\Delta$  and  $\delta$ .

$$\tan\theta = \delta/\Delta \quad (1)$$

It is assumed that the PT tendon has an axial stiffness of  $k_{pt}$ . The force in the PT tendon can be calculated using Equation 2.

$$F_{pt} = F_{pt}^0 + k_{pt} \cdot \Delta \cdot \tan\theta \quad (2)$$

where  $F_{pt}^0$  is the initial pretension force of the PT tendon.



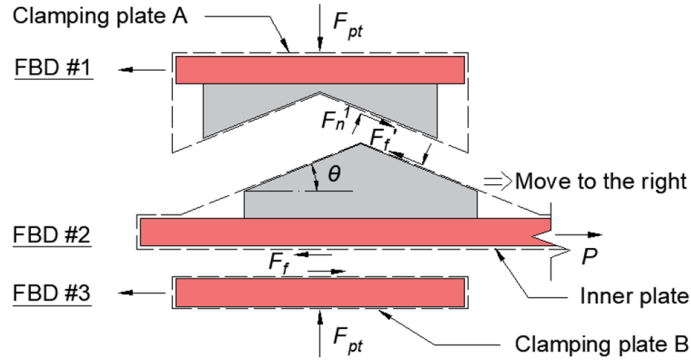
**Figure 2.2 Clamping plate A opens as the inner plate moves**

Figure 2.3 shows the free body diagram of the SCFD, when the inner plate is pulled from left to right. In this figure,  $P$  is the external force.  $\theta$  is the slope angle of the cone which is limited from 0 to 90 degrees.  $F_f$  and  $F_f'$  are the friction forces at the flat and cone surfaces, which can be calculated using Equation 3 and 4, respectively.

$$F_f = \mu \cdot F_{pt} \quad (3)$$

$$F_f' = \mu' \cdot F_n^1 \quad (4)$$

where  $\mu$  is the friction coefficient between the friction pad and the steel plate;  $\mu'$  is the friction coefficient between conical surfaces;  $F_n^1$  is the normal contact force on cone surface.



**Figure 2.3** Free body diagram as the inner plate moves to the right

Using FBD 2, Equation 5 shows the force equilibrium in vertical direction. Substituting Equation 4 into Equation 5, Equation 6 shows the normal force  $F_n^1$  as a function of the pretension force  $F_{pt}$ .

$$F_f' \cdot \sin\theta - F_n^1 \cdot \cos\theta + F_{pt} = 0 \quad (5)$$

$$F_n^1 = \frac{F_{pt}}{\cos\theta - \mu' \cdot \sin\theta} \quad (6)$$

Because the normal force  $F_n^1$  must be positive, otherwise the SCFD will get detached. In addition, the pretension force  $F_{pt}$  is always positive, this means the denominator  $\cos\theta - \mu' \cdot \sin\theta$  must be positive. By rearranging the constraints, Equation 7 gives the relation between the slope angle and the friction coefficient on the cone surface.

$$\mu' < \frac{1}{\tan\theta} \quad (7)$$

Using FBD 2, Equation 8 shows the force equilibrium in horizontal direction. Substituting Equation 1, Equation 2 and Equation 4 into Equation 6, Equation 9 gives the external force  $P$  as a function of the pretension force  $F_{pt}$ .

$$P - F_f - F_f' \cdot \mu' \cdot \cos\theta - F_n^1 \cdot \sin\theta = 0 \quad (8)$$

$$P = F_{pt} \cdot B1 = (F_{pt}^0 + k_{pt} \cdot \Delta \cdot \tan\theta) \cdot B1 \quad (9)$$

where  $B1 = \left( \frac{\tan\theta + \mu'}{1 - \mu' \cdot \tan\theta} + \mu \right)$ .

The initial sliding force,  $P_0$ , can be calculated using Equation 9 by setting  $\Delta = 0$ . Equation 10 shows the initial sliding force. Similarly, the maximum sliding force,  $P_m$ , can be calculated using Equation 9 by setting  $\Delta = \Delta_m$ , where  $\Delta_m$  is the maximum deformation of the SCFD. Equation 11 shows the maximum sliding force.

$$P_0 = F_{pt}^0 \cdot B1 \quad (10)$$

$$P_m = (F_{pt}^0 + k_{pt} \cdot \Delta_m \cdot \tan\theta) \cdot B1 \quad (11)$$

The post yield stiffness of the SCFD can be calculated using Equation 12.

$$k_p = \frac{P_m - P_0}{\Delta_m} = k_{pt} \cdot \tan\theta \cdot B1 \quad (12)$$

If the SCFS reverses the direction (moves from right to left), the friction forces will reverse in sign.

Figure 2.4 shows the free body diagram of the SCFD when the displacement reverses.

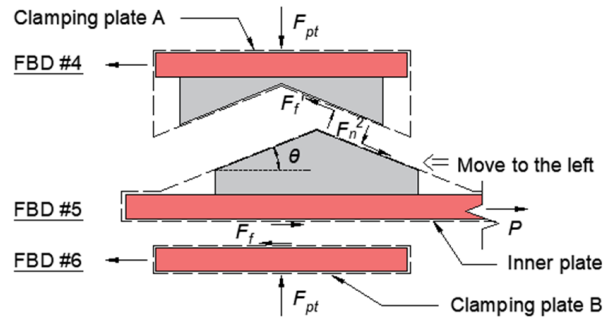


**Figure 2.4 Free body diagram as the inner plate moves to the left**

Using FBD 5, the vertical and horizontal equilibrium can be summarized in Equation 13 and 14, respectively.

$$-F_f' \cdot \sin\theta - F_n^2 \cdot \cos\theta + F_{pt} = 0 \quad (13)$$

$$P + F_f + F_f' \cdot \mu' \cdot \cos\theta - F_n^2 \cdot \sin\theta = 0 \quad (14)$$

Similarly, using FBD 4 and FBD 5, the updated normal force  $F_n^2$  and external force  $P$  can be calculated using Equation 15 and Equation 16, respectively.

$$F_n^2 = \frac{F_{pt}}{\cos\theta + \mu' \cdot \sin\theta} \quad (15)$$

$$P = (F_{pt}^0 + k_{pt} \cdot \Delta \cdot \tan\theta) \cdot B2 \quad (16)$$

Where  $B2 = \left( \frac{\tan\theta - \mu'}{1 + \mu' \cdot \tan\theta} - \mu \right)$ .

When  $\Delta = \Delta_m$ , the unloading force,  $P_u$ , can be calculated using Equation 18. Equation 19 shows the unloading force.

$$P_u = (F_{pt}^0 + k_{pt} \cdot \Delta_m \cdot \tan\theta) \cdot B2 \quad (19)$$

When  $\Delta = 0$ , the residual force,  $P_r$ , can be calculated using Equation 18. Equation 20 shows the residual force.

$$P_r = F_{pt}^0 \cdot B2 \quad (20)$$

The unloading stiffness of the SCFD can be calculated using Equation 21.

$$k_u = \frac{P_u - P_r}{\Delta_m} = k_{pt} \cdot \tan\theta \cdot B2 \quad (21)$$

Since  $F_{pt}$ ,  $k_{pt}$ , and  $\tan\theta$  are always positive,  $B2$  will govern the sign of the unloading force  $P_u$ , the residual force  $P_r$  and the unloading stiffness  $k_u$ . If  $B2$  is positive, both the unloading force, residual force and unloading stiffness will be positive and vice versa. Equation 22 shows the critical angle,  $\theta_{critical}$ , as the function of  $\mu$  and  $\mu'$ . If  $\theta > \theta_{critical}$ ,  $B2$  will be positive. If  $\theta < \theta_{critical}$ ,  $B2$  will be negative. Similarly,  $\theta = \theta_{critical}$ ,  $B2$  will be zero.

$$\theta_{critical} = atan\left(\frac{\mu + \mu'}{1 - \mu \cdot \mu'}\right) \quad (22)$$

Figure 2.5a shows SCFD hysteresis type I under the condition where  $B2$  is positive; Figure 2.5b shows SCFD hysteresis type II under the condition where  $B2$  is zero; Figure 2.5c shows SCFD hysteresis type III under the condition where  $B2$  is negative. It should be note that SCFD can center itself under all these three cases.

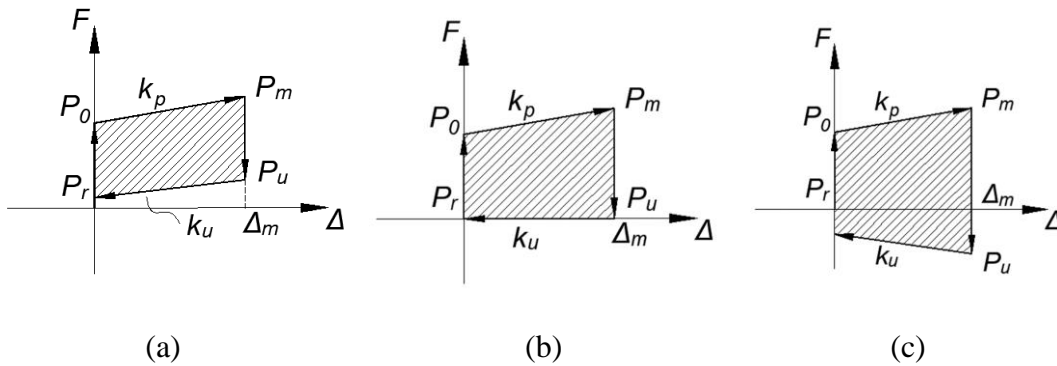


**Figure 2.5 Three different types of hysteresis (a) Type I (b) Type II (c) Type III**

## 2.2 Design Criteria for SCFD

All components of SCFD need to be capacity designed. The shear plates and clamping plates are supposed to remain elastic all the time. Slip critical connection determines the size of end plates and the configuration of bolt group. The most important one is the design of PT tendons, which governs the secondary stiffness and the deformation capacity.

In this study, Belleville washer is used as the PT tendons. Belleville washer is in cone shape, which allows it to gradually become flat as the force goes. Like springs, Belleville washer is designed to have individual stiffness ( $k_{ws}$ ), load capacity and deformation capacity. These all depend on the way it is stacked. Washers are normally stacked in two ways: in series and in parallel. The force

capacity of the washers is given in Equation 23. The deformation capacity of the washers is given in Equation 24.

$$P_{capacity} = n_p \cdot P_{ws} \quad (23)$$

$$\delta_{capacity} = n_s \cdot \delta_{ws} \quad (14)$$

Where  $P_{ws}$  is the flat load of one single washer;  $n_p$  is the number of washers stacked in parallel;  $n_s$  is the number of washers stacked in series ;  $\delta_{ws}$  is the flat deformation of one single washer.

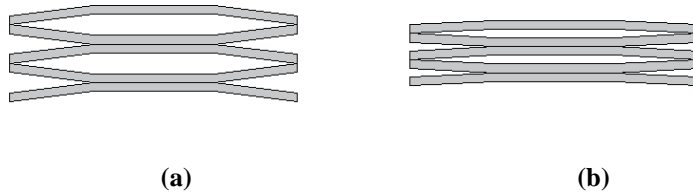


**Figure 2.6 Belleville washer mechanism (a) No deformation (b) Under compression**

The effective stiffness is simply calculated using the ratio of force capacity to deformation capacity, as is shown in Equation 25.

$$k_e = \frac{P_{total}}{\delta_{total}} = \frac{n_p \cdot P_{ws}}{n_s \cdot \delta_{ws}} = \frac{n_p}{n_s} \cdot k_{ws} \quad (25)$$

When designing the washers, it is important to consider the initial deformations due to the pre-tensioning of bolts. Accounting for the deformation required in bolt pretension, the total demand is obtained in Equation 26, thus the total force demand is obtained in Equation 27. The washers should always be designed to meet the demands, otherwise infinite stiffness comes after washers become flat.

$$\delta_{demand} = \frac{F_{pt}}{k_e} + \Delta_m \cdot \tan\theta < \delta_{capacity} \quad (26)$$

$$P_{demand} = F_{pt} + \delta_{demand} \cdot k_e < P_{capacity} \quad (27)$$

## 2.3 Equation Verification through Finite Element Model in Abaqus

To visualize the motion of SCFD and verify the equation, a finite element model was developed in Abaqus. There are two main purposes in this section: confirm that SCFD can deform as is designed when it is subjected to external loading; make sure the theoretical equations derived in the last section can give a reasonable prediction on essential design forces and stiffnesses. In the numerical model presented here, all dimensions and parameters are designed to be realistic values.

### 2.3.1 Overview of Finite Element Model

This numerical model is composed of 3D finite elements and 3D analytic rigid elements. Except the female cone, all other parts are modeled using 3D finite elements. Because there are numerical convergence issues when line contact or point contact occurs between two finite element parts. To simulate the contact between conical surfaces, 3D analytic rigid element is adopted for the female cone. 3D analytic rigid element is only involved in getting resultant forces, not in numerical check for convergence. Figure 2.7 shows that both models are generated through section revolving about the center axis. Later the male cone will be assembled onto the female cone to create the contact between conical surfaces.

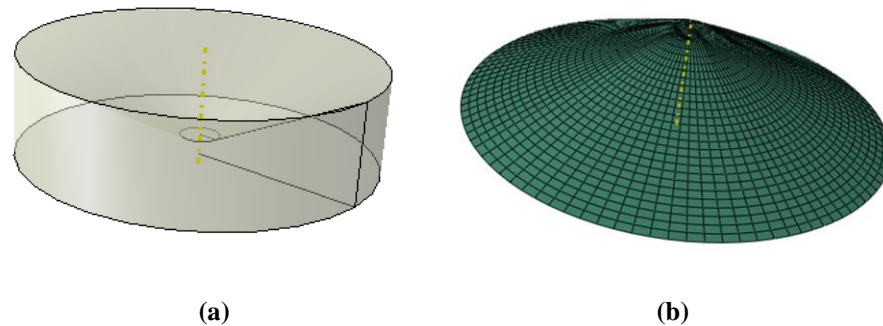


**Figure 2.7** Pair of cones modeled in Abaqus : (a) Female cone - rigid element (b) Male cone - finite element

Figure 2.8 shows the assembled Clamping plate A including the steel plate with two slot holes and one female cone. Since the female cone should be either welded or bolted to the base steel plate,

in the modeling, female cone is connected to the base steel plate using “Tie” constraint. All the forces will be fully transferred.

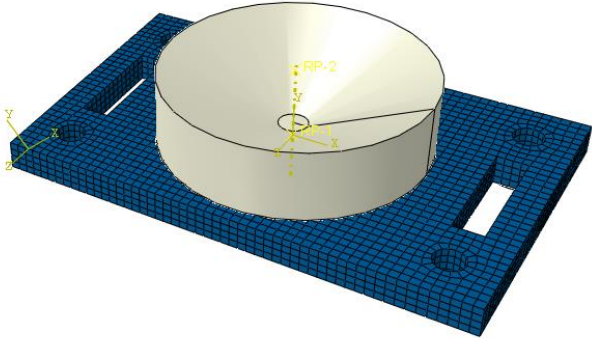


**Figure 2.8 Clamping plate A**

Figure 2.9 shows the outer clamping pate B. The inner steel plate is simplified into the red circular pad in the simulation. Two grey parts represent the stoppers. All the parts are connected to each other through “Tie” constraint to have fully transferred forces. The flat friction surface is at the top of the red friction pad. During the assembly, this surface will have contact with the flat surface of the male cone such that the male cone will move against the red pad.

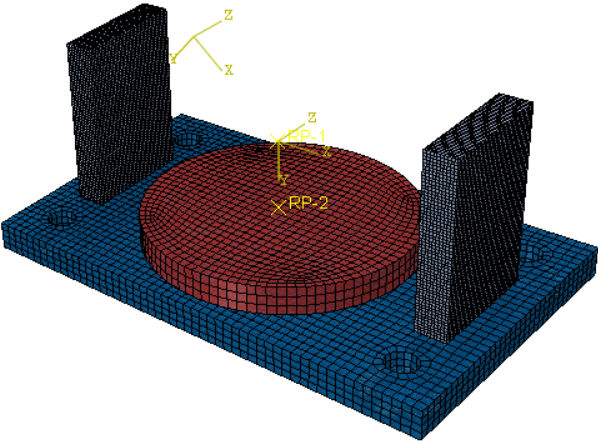


**Figure 2.9 Clamping plate B**

Figure 2.10 shows the assembled SCFD simulated in ABAQUS. The male cone is sandwiched by outer clamping plate A and B. In the proposed damper model, the male cone is attached to the

inner plate. However, it is not included here to simplify the model. The male cone itself has both conical surface and flat surface. In addition, truss wire is adopted in the numerical model to simulate the combined behavior of bolt and post tension tendons. The wire is pretensioned by setting the temperature field to have a negative value in the very first step, which is known as temperature load. To calculate such temperature load, cross area ( $A$ ), elastic modulus ( $E$ ), coefficient of thermal expansion ( $\alpha$ ) and change of temperature ( $\Delta T$ ) are required. As the temperature goes negative, the wire tends to shrink. Due to the boundary restraint, pretension force is generated inside the wire, thus both clamping plates are subjected to normal pressures transferred from the wires. Equation 28 shows the pretension force calculation. Equation 29 gives the corresponding stiffness ( $K$ ) as a function of the wire elastic modulus ( $E$ ), wire area ( $A$ ) and its own length ( $L$ ). Later the temperature is set as constant till end of the analysis. As the male cone moves against the female cone, the outer clamping plate A will move outwards and stretch the wires. Then the axial force along the wire will increase proportionally to the extension.

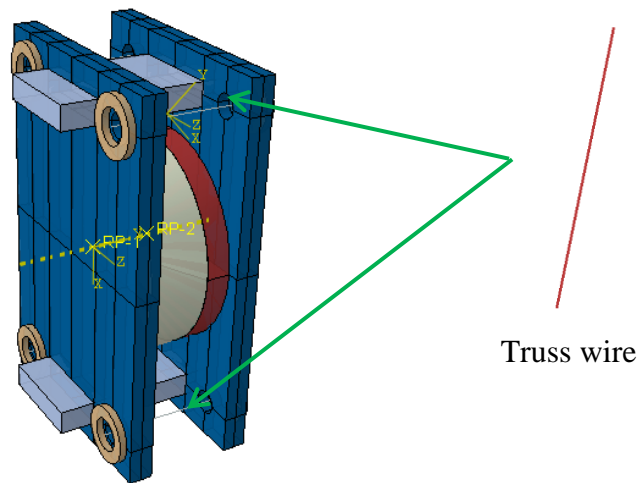


**Figure 2.10** Assemble view in Abaqus

$$F = A \cdot E \cdot \alpha \cdot \Delta T \quad (28)$$

$$K = \frac{A \cdot E}{L} \quad (29)$$

There are three different contact surfaces to define (Figure 2.11): the flat friction surface, the conical friction surface, and surfaces between stoppers and the clamping plate B. In terms of the normal behavior of the contact surface, they are all defined to have “Hard contact”, which means there is no intrusion act. In terms of the tangent behavior of the contact surfaces, contact between stoppers and the clamping plate B is defined to be frictionless, while other two types of contact is using “Penalty friction formulation”. Different friction coefficients are assigned to these two contacts respectively.

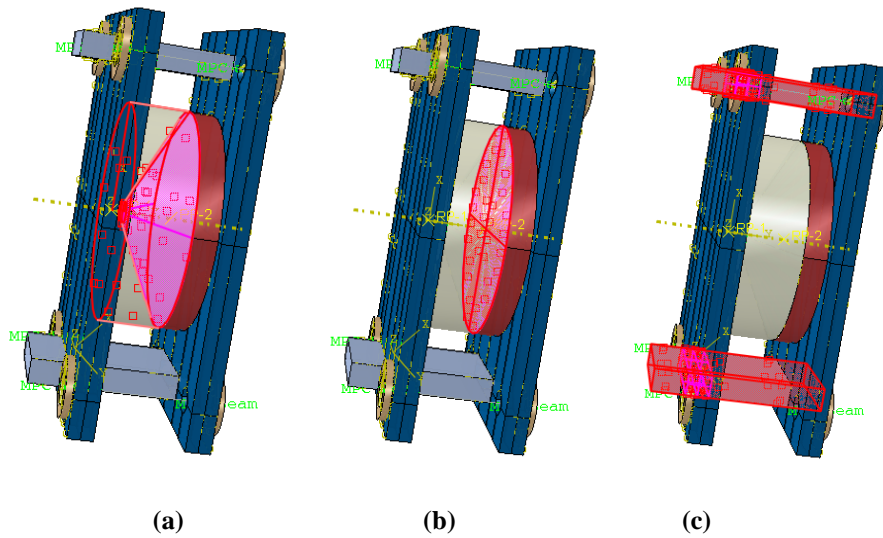


**Figure 2.11 Three different contact surfaces: (a) Conical contact surface (b) Flat contact surface (c) Stopper-Clamping plate contact surface**

The clamping plate A is defined to have fixed boundary condition. On top of that, the corresponding side of four wires is also set to be fixed, while another end of four wires is free in Y direction. Y direction is also the direction the clamping plate A will open along the stoppers as

the male cone moves against the female cone. In this way, the stiffness of the wire can engage in the analysis as soon as it is stretched by the clamping plate A. The loading reference point is located on the center of male cone flat surface. One full cycle is applied to the loading reference point in X direction.

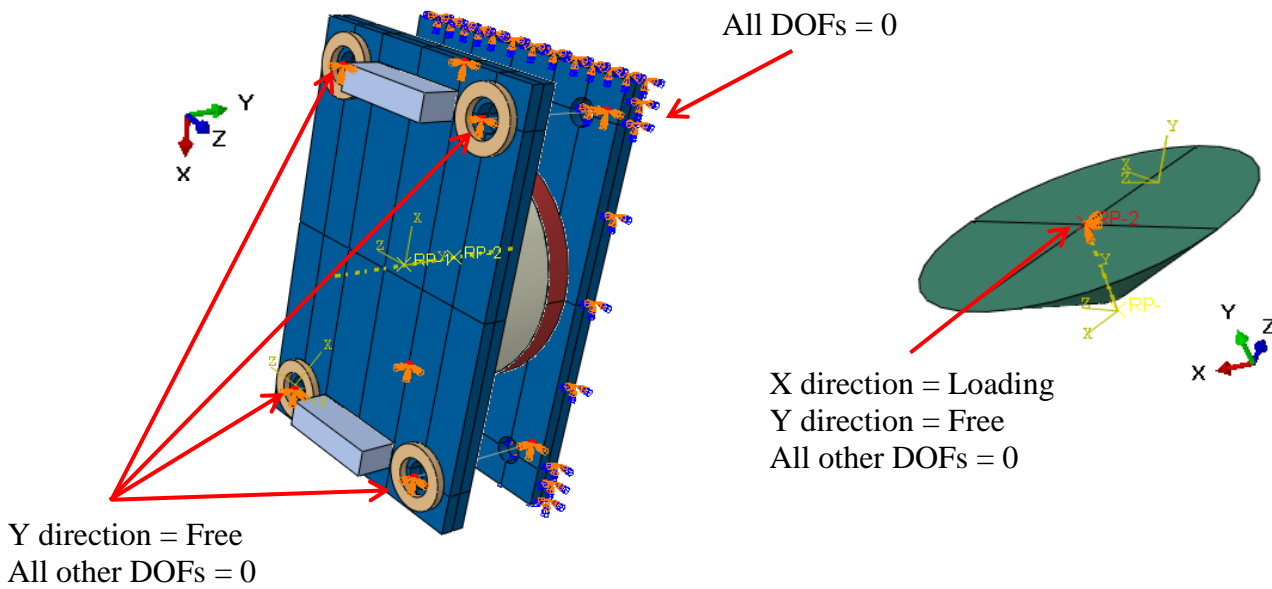


Figure 2.12 Summary of boundary conditions

### 2.3.2 Motion Observation & Equation Verification

Figure 2.13 shows two different stages: one at maximum deformation to the right and one at maximum deformation to the left. As was proposed, the clamping plate A will move outwards along the stoppers as the male cone moves against the female cone. During the time, the post tension tendon, modeled using wire here, deforms and introduces more normal pressure. Thus, the total reaction force increases proportionally to the global deformation. The same parameters are applied to the equations. Figure 2.14 shows the comparison between the predicted hysteresis and the simulated hysteresis. It shows that all essential points are well matched.

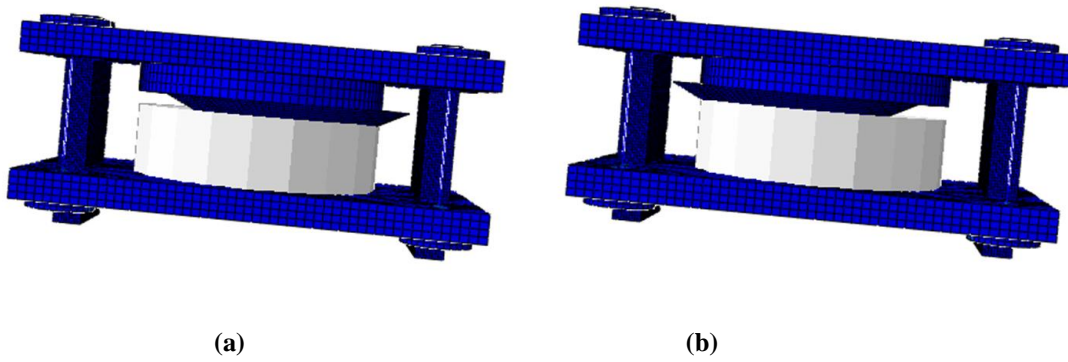


Figure 2.13 Motion examples (a) Max to the right (b) max to the left

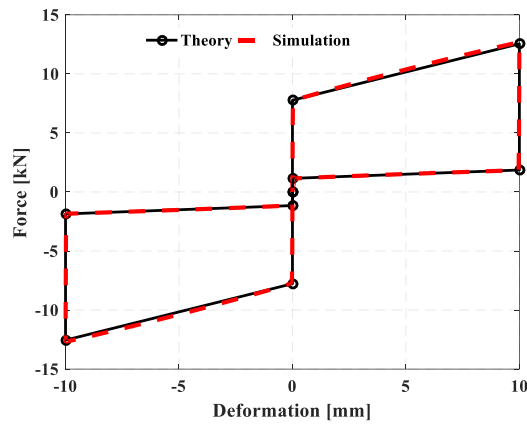


Figure 2.14 Comparison between theory and simulation

## 2.4 Summary

The concept of SCFD was presented first: use of cone shape, PT tendons and isolating the bolts help achieve the goal of self-centering and all directional motion. Then the theoretical equations were developed, critical conditions were discussed. Three types of hysteresis were proposed. Especially, it was concluded that all of them have self-centering capability. In the end, numerical model was successfully developed, and the mechanism was briefly verified through ABAQUS simulation.

## **Chapter 3: Component Experiment of SCFD**

One prototype damper was built for the experimental test. Parameter study was carried on this one prototype because SCFD is designed to be damage free. The tests were conducted at the Structural Lab, University of British Columbia, Vancouver. The main purpose of the experiment is to validate the proposed behavior and investigate how the behavior changes as design parameters are changed. More parameter study will be presented in Chapter 4 as the theoretical equation was verified in this chapter, which introduces the test setup, specimen design, instrumentation, controller and loading protocol.

### **3.1 Test Setup**

The test setup designed by Winda (2018) at University of British Columbia was adopted in this study. This setup was designed to test specimen subjected to shear deformation. One feature of this setup is that the axial constrain is eliminated, which prevents the extra axial force from being generated. There are five main components in this setup (Figure 3.1): the loading beam, pantograph, mounting frame, out-of-plane support and the fin extension. The out-of-plane support and the fin extension can prevent the loading beam from rotating out of plane. The pantograph can provide translation degree of freedom in U2 direction and prevent the loading beam from rotating in plane as well. The center line of the actuator was designed to be lined up to the center of the specimen in order to minimize the extra moment brought by eccentricity, thus the force demand on the pantograph was brought down. The actuator has a capacity of 1000kN and a stroke of +/- 150mm. Displacement control was adopted to move the loading beam in U1 direction.

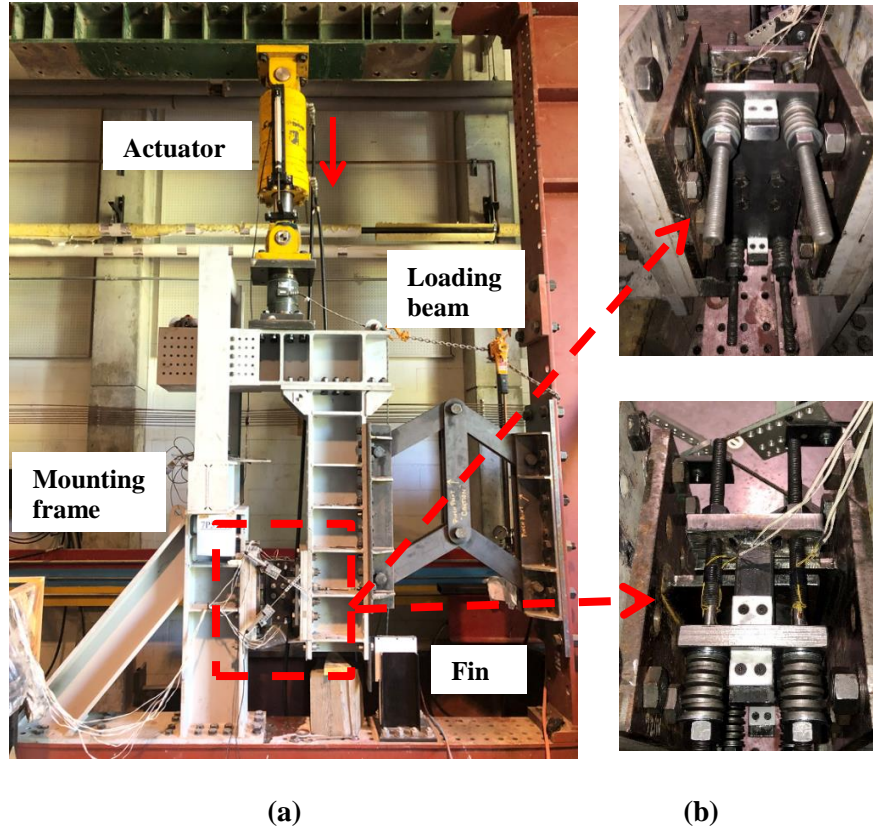


**Figure 3.1 Test setup and the specimen installed (a) Set up (b) Back & top view of the specimen**

### **3.2 Specimen and Testing Matrix**

All the components of the specimen were designed to keep elastic during the test. Table 3.1 presents a summary of essential design parameters. The following shows all the component detailing of the prototype. All the components were fabricated by George Third and Son. All steel material is A36 steel except the pair of cones. The detailed fabrication drawings are shown in Appendix A.

**Table 3.1 Design Parameters**

Parameter	Value
$\theta$	22
$\mu$	0.03
$\mu'$	0.3
Belleville Washer Dish [mm]	1.2
Belleville Washer Stiffness [kN/mm]	33

1. Clamping plate A with female cone

Clamping plate A has two rectangle holes on top and bottom, which allows itslef slide along the steel stoppers on clamping plate B. In addition, a female cone was also attached to clamping plate B through bolt connection. Instead of using A36 steel, stainless steel was used for the fabrication of cones. Stainless steel brings smoother surface, reducing the friction between conical surfaces. The steel base plate was designed to resist the moment contributed by PT forces.



**Figure 3.2 Clamping plate A with female cone**

2. Clamping plate B with stoppers

Figure 3.3 shows an assemble piece including clamping plate B and the end plate. End plate was designed as an adaptor to match the hole pattern on the setup. In the test setup,

this entire piece will be bolted to the mounting frame. The smaller steel plate was welded to the end plate with an offset from the middle, which leaves the room for a Teflon sheet. Teflon sheet was used as the friction pad to reduce the friction and was bolted to the steel plate. Teflon surface will have contact against the flat side of the inner plate. On the other side of the smaller steel plate, the clamping plate B was bolted to it. Additionally, Teflon sheets were attached to the steel stoppers surfaces to reduce the potential friction between the stopper and the clamping plate A when the clamping plate moves outwards along the stoppers.



**Figure 3.3 End plate and clamping plate B**

### 3. Inner plate

Figure 3.4 shows the inner plate welded to another end plate. The inner plate has one male cone bolted on. According to the test plan this entire piece will be bolted to the loading frame, as the actuator pushes the loading frame, the inner plate will move downwards; as the actuator pulls the loading frame, the inner plate will move upwards. Although there is no constrain in out of plane direction, the inner plate won't move horizontally. In horizontal direction, male cone has to be lined up to the female cone from the beginning of the test.



**Figure 3.4 Steel plate with male cone**

#### 4. High strength bolt and Belleville washers

Four high strength bolts were used in the test to. Normal force is generated by pretensioning the bolts. They will be pretested in a tensile test to calibrate the strain gauges glued on the surface. Belleville washers provided by ATP were used in the test. Hence, PT tendons in SCFD is composed of high strength bolt and stacked Belleville washers. When washers work under huge pressure, they will lose deformation capacity due to high stress concentration. It is recommended to record the change of individual washer depth after every test.



**(a)**



**(b)**

**Figure 3.5 (a) High strength bolts (b) Belleville washers**

To verify the hysteretic behavior of SCFD, a series of experimental tests were carried out using a prototype SCFD. The cones were manufactured using stainless steel, where the friction coefficient is estimated between 0.2 – 0.4 (Barrett et al. 1990). In this study the 0.3 was used and calibrated from the experimental data. To reduce the friction force between the inner plate and clamping plate B, Teflon sheet was added. Typical friction coefficient between steel and Teflon is between 0.01 – 0.2 (Barrett et al. 1990) . In this study,  $\mu'$  is selected and calibrated to be 0.03. In this study, Belleville washers used as the PT tendons. Different combinations of the Belleville washers were used. Table 3.2 shows the stiffness and initial tensioning force of PT tendons. Due to the cost of the manufacturing, only one cone with an angle of 22 degrees is selected.

**Table 3.2 Testing Matrix**

Specimen	Pretension Force	PT tendon stiffness
	$F_{pt}^0$ [kN]	$k_{pt}$ [kN/mm]
P5W8	5	16.4
P8W8	8	16.4
P10W8	10	16.4
P5W10	5	13.2
P8W10	8	13.2
P10W10	10	13.2
P5W12	5	11.0
P8W12	8	11.0
P10W12	10	11.0

### 3.3 Instrumentation

#### 3.3.1 Load Feedback

To capture the load the specimen was subjected to, one load cell (MTS 661.31) with a capacity of 100kN was installed between the actuator and the loading beam using bolt connections. From the load cell, the load feedback can be directly read from the controller.

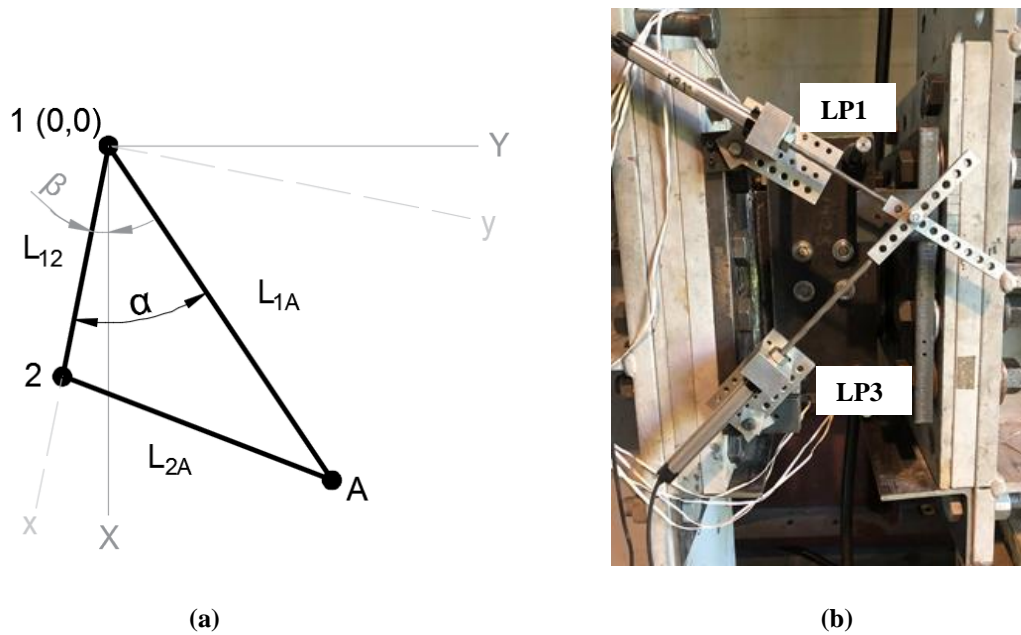


Figure 3.6 Actuator and load cell

#### 3.3.2 Displacement Feedback

To track the displacement in U1 direction, there is one simple approach: using the linear pot attached at the actuator. However, slippage happening at all the bolt connections will bring many unexpected errors such that the real deformation of the specimen is less than the deformation of the actuator. To minimize the such error, there are two alternative approaches: one is to place one linear pot at the bottom of the loading beam, as the loading beam moves the bottom end will deform

the linear pot and displacement feedback can be obtained; another one is to have a virtual sensor, which can provide the local deformation of the specimen. Having a linear pot at the bottom is not a reliable way. Therefore, the methodology of using virtual sensor was adopted in this test, which was proposed by Winda (2017). In this methodology, two linear pots were used to capture the movement of their intersection in plane. Both are calibrated before the test and the calibrations are shown in Appendix B. As is shown in Figure 3.7, L1A (LP1 in the test) and L2A (LP3 in the test) represent two linear pots. Point 1 and point 2 are mounted to the fixed side of the specimen. L12 represents the distance between two mounting points. Point A was mounted to the free side of the specimen. Both linear pots have their original reading. From their real-time reading, the difference was obtained as the deformation happening to two linear pots, which was used to calculate the position change of Point A in plane. Then the change of position in U1 direction was used as the displacement feedback to the controller. Data records of LP1 and LP3 during the test are shown in Appendix C.



**Figure 3.7 (a) Concept of getting displacement feedback (b) Linear pots configuration**

### 3.3.3 Pretension Force Feedback

To accurately reach the pretension force designed for each bolt, strain gauges were placed on the bolts to track the force change. In order to balance the error, two gauges were glued to two opposite surfaces. Because the data acquisition system can only provide voltage reading. It is necessary to have calibration conducted such that voltage reading can be converted to actual pretension force in each bolt. Therefore, four tensile tests were carried out for each bolt to map the voltage reading to pretension force. The tensile tests were finished using the Baldwin Machine at University of British Columbia. Four corresponding calibration results were shown in the Appendix D. Data records of four sensors, named SG0, SG1, SG2, SG3 respectively, are shown in Appendix E.

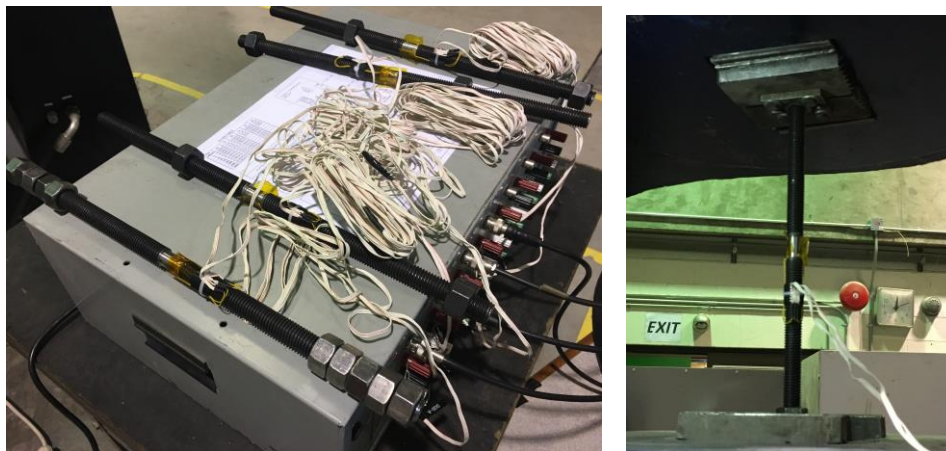


Figure 3.8 Condition box and bolt in tensile test

### 3.4 Controller and Loading Protocol

ACTS controller was adopted in the test. By using displacement control and PID algorithm, actuator can be successfully controlled from the virtual sensor feedback. Loading protocol recommended in ATC-24 (1992) was used in the test. Because SCFD is a friction based damper, the sliding happens right after the external force reaches the designed sliding force, which makes the “yielding deformation” to be zero. Instead of using yielding deformation to define all the

amplitudes in the loading protocol, the maximum amplitude was set to be the maximum displacement tested in the experiment, then all other ones were determined relative to the maximum value. In the test, the maximum deformation in U1 direction was 6mm. The updated loading protocol was shown in Figure 3.10.



**Figure 3.9 ACTS controller**

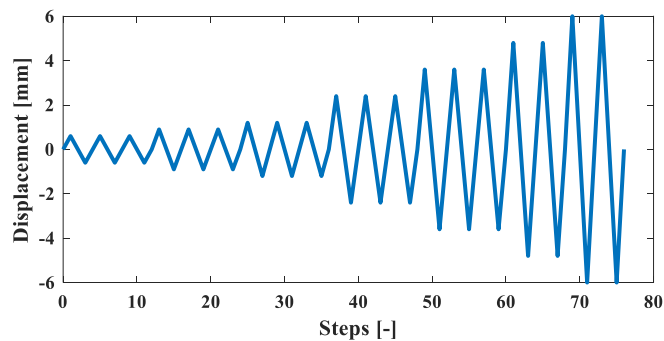


**Figure 3.10 Loading protocol**

### **3.5 Summary**

This Chapter presented a detailed discussion on test setup, prototype specimen, instrumentation and test plan. The vertical loading-no axial constraint set up in UBC was adopted for this test. According to the proposed mechanism and developed methodology, prototype specimen was designed and fabricated. There are nine tests completed using nine different combinations of two main parameters (pretension force and PT tendon stiffness) respectively.

## **Chapter 4: Experiment Results and Parameter Study**

Experimental results of nine tests are presented in this chapter. The influence the PT stiffness & strength has on hysteresis behavior has been documented. Proposed theoretical equation was also verified against the corresponding test results. In addition, capacity of energy dissipation was also discussed. There were only two parameters studied in the experiment. More parameter studies were conducted using the theoretical equations in order to fully understand how the hysteresis behavior varies with different design parameters, which can help produce better design in further applications.

### **4.1 Experimental Results**

#### **4.1.1 Overview of Test Results**

P5W8 has a pretension force of 5kN and eight washers in series. It is found in the test that the slipping force is about 5.1 kN and the maximum force is about 24.54 kN. The post stiffness is about 3.24 kN/mm. In positive direction, it is pushed to 6mm as is planned. However, in the opposite direction, it is only pushed to 5.5mm as can be observed from the figure. This is because the change of direction was proceeded earlier before it reached the designed deformation. P8W8 has a pretension force of 8kN and eight washers in series. It is found in the test that the slipping force is about 9.1 kN and the maximum force is about 29.08 kN. The post stiffness is about 3.33 kN/mm. As the number of washers is the same, the effective stiffness doesn't change, which leads to similar post stiffness. P10W8 has a pretension force of 10kN and eight washers in series. It is found in the test that the slipping force is about 10.8 kN and the maximum force is about 31.8 kN. The post stiffness is about 3.5 kN/mm. P5W10 has a pretension force of 5kN and ten washers in series. It is found in the test that the slipping force is about 5.9 kN and the maximum force is about 21.98 kN. The post stiffness is about 2.68 kN/mm. P8W10 has a pretension force of 8kN and ten

washers in series. It is found in the test that the slipping force is about 8.4 kN and the maximum force is about 25.32 kN. The post stiffness is about 2.82 kN/mm. P10W10 has a pretension force of 10kN and ten washers in series. It is found in the test that the slipping force is about 10.3 kN and the maximum force is about 27.28 kN. The post stiffness is about 2.83 kN/mm. P5W12 has a pretension force of 5kN and twelve washers in series. It is found in the test that the slipping force is about 5.2 kN and the maximum force is about 17.2 kN. The post stiffness is about 2 kN/mm. It is clearly seen that the maximum force is brought down. P8W12 has a pretension force of 8kN and twelve washers in series. It is found in the test that the slipping force is about 8.3 kN and the maximum force is about 20 kN. The post stiffness is about 1.95 kN/mm. P10W12 has a pretension force of 10kN and twelve washers in series. It is found in the test that the slipping force is about 11.5 kN and the maximum force is about 24.94 kN. The post stiffness is about 2.24 kN/mm.

#### **4.1.2 Summary of Experimental Results and Verifications of Equations**

Figure 4.1 summarizes nine experimental results: every row has the same number of washers, while every column has the same amount of pretension force. It is clearly shown that the sliding force and the ultimate force increases as the pretension force increases. When it comes to the remaining force and residual force, there is an uplift of the bottom line, which means more pretension force brings better self-centering feature. However, it is not very sensitive to the change of pretension force. More washers bring the loading and unloading stiffness down, which leads to lower ultimate forces when the sliding force is the same. Furthermore, Figure 4.2 shows that in general, when the pretension force increases the sliding force ( $P_0$ ), maximum force ( $P_m$ ), unloading force ( $P_u$ ) and residual force ( $P_r$ ) will increase; as the PT stiffness decrease, the loading and unloading stiffness will decrease. In addition, post stiffness is independent on the change of

pretension force and the sliding force is independent on the change of PT tendon stiffness. By adopting the same parameters, Figure 4.1 also provides the comparison between the predicted hysteresis against the experimental results. It shows that SCFD behavior is well predicted by theoretical equations derived in Chapter two. Thus, the mechanism is verified, thus can be used to conduct further parameter study.

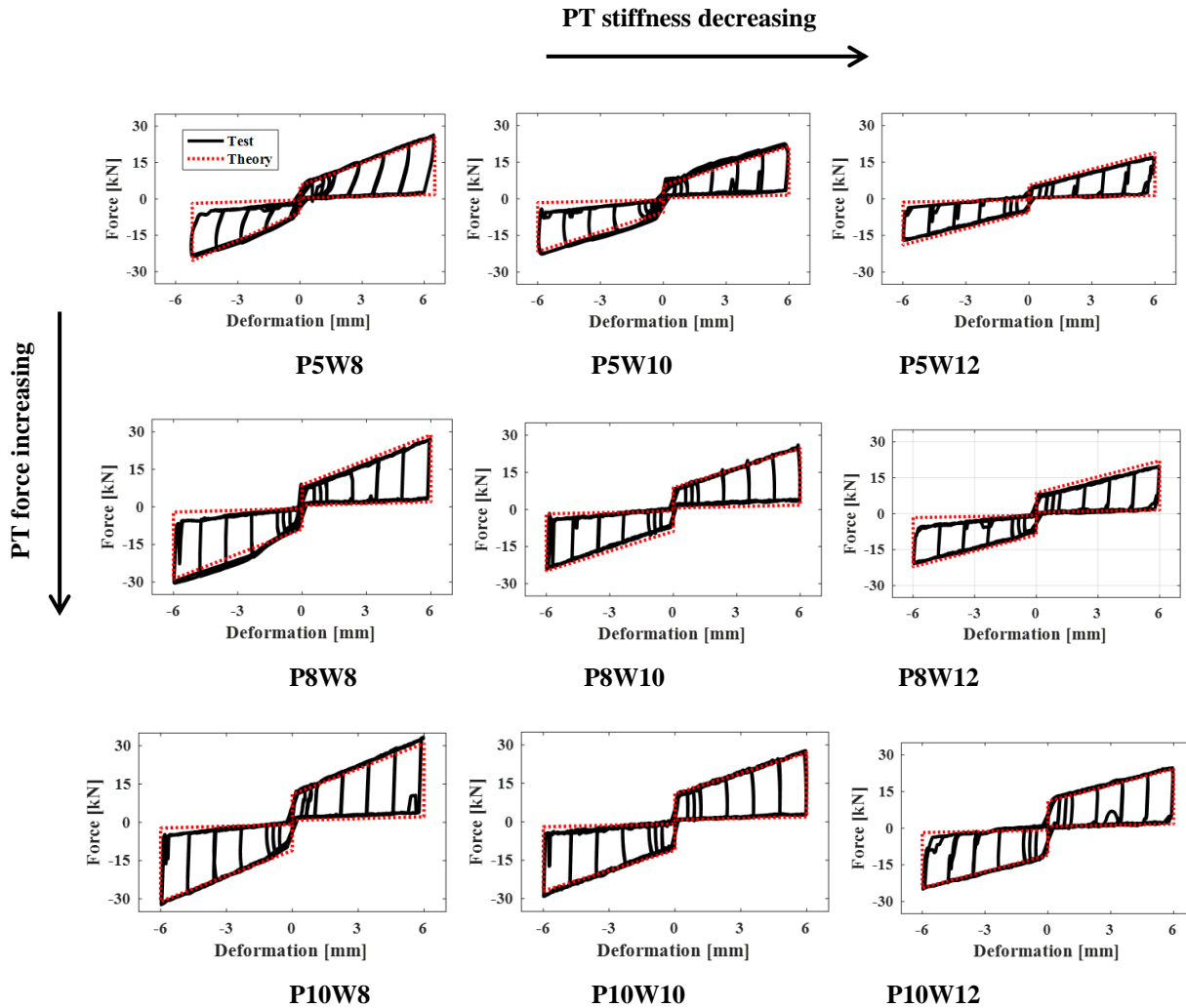
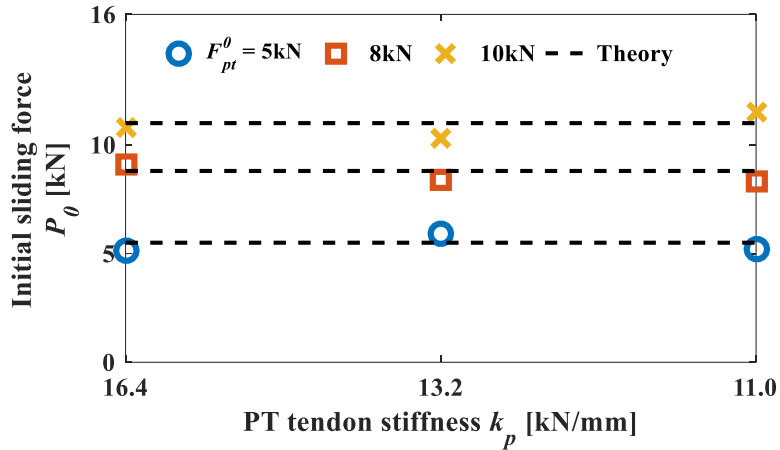
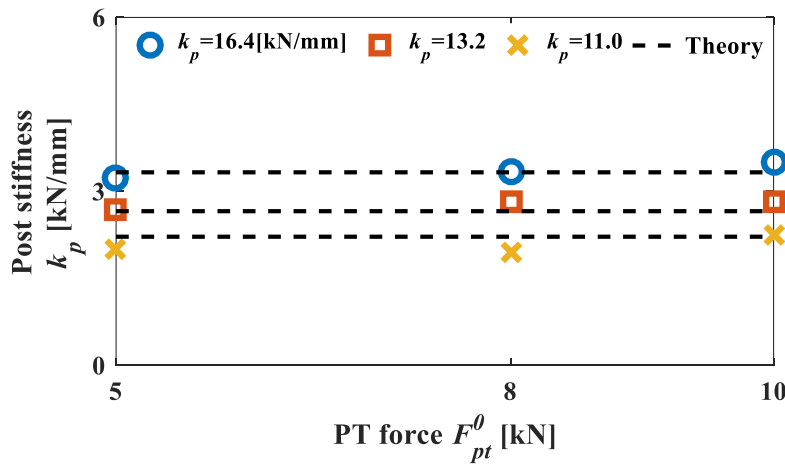


Figure 4.1 Experimental results



(a)



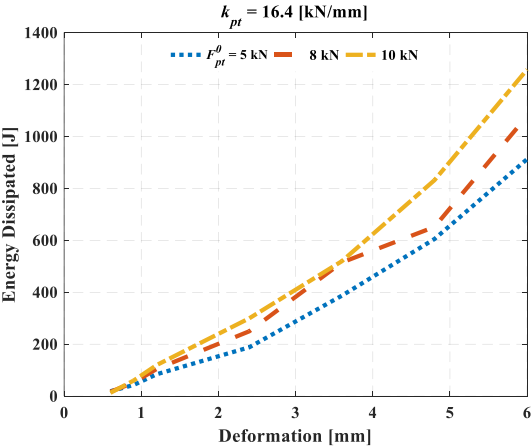
(b)

Figure 4.2 Sensitivity check on (a) sliding force (b) post stiffness

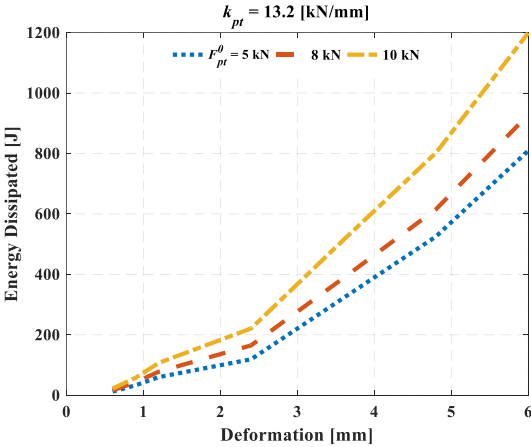
### 4.1.3 Discussion on Energy Dissipation

Figure 4.3 shows the cumulative energy dissipation of each specimen. First figure shows cases where there are eight washers in series and the PT tendon stiffness is about 16.4 kN/mm. There are three different scenarios and each line represents one pretension scenario: 5kN, 8kN and 10kN. It shows that energy dissipation increases as the deformation increases. Especially, as deformation comes to the maximum deformation, the rate change of energy dissipation has increment as well.

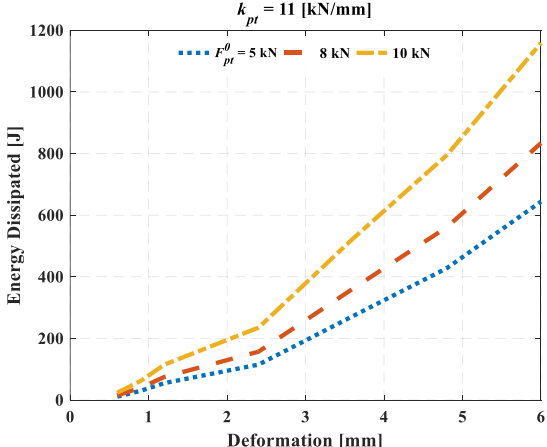
It also shows that more pretension force leads to better energy dissipation capability. The second and the third figure show these same scenarios as well, except that in the second figure, there are ten washers in series and the corresponding stiffness is 13.2 kN/mm, while in the third figure, there are twelve washers in series and the corresponding stiffness is 11 kN/mm. Overall, similar trend can be observed.



(a)



(b)



(c)

Figure 4.3 Cumulative energy dissipation of different specimens over the test

Figure 4.4 summarizes total energy dissipation obtained in all nine tests. The energy dissipation is plotted against the magnitude of the pretension force. Three lines represent the specimen having PT stiffness of 16.4 kN/mm, 13.2 kN/mm and 11 kN/mm, respectively. It shows that the total amount of energy dissipation increases as the number of washers decreases or as the pretension magnitude increases. In addition, as pretension force goes up, the energy dissipation becomes less sensitive to the number of stacked washers because the figure shows less difference between three different values. This can be explained by considering the ratio of post tension stiffness to the pretension force magnitude. When higher pretension force is applied, such ratio will decrease, thus leading to less change in energy dissipation capability as the PT tendon stiffness varies.

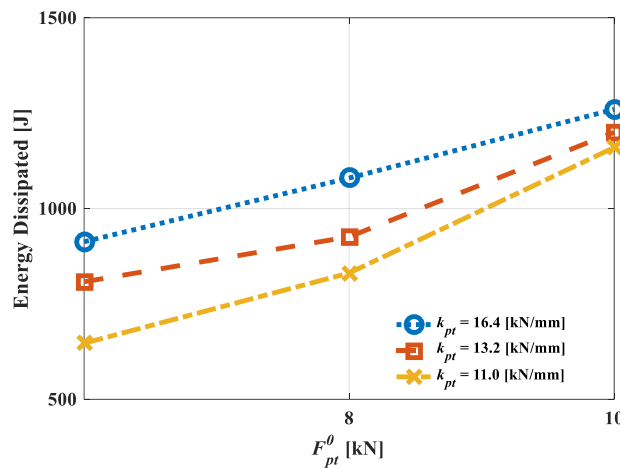


Figure 4.4 Energy dissipation plot against the pretension force and the number of washers

## 4.2 Parameter Study

Based on the validated mechanical model presented, a detailed parameter study is conducted to examine influence of the sliding force ( $P_0$ ), post yield stiffness ( $k_p$ ) and the unloading stiffness ( $k_u$ ) of the SCFD. In this study, the friction coefficient between flat plates ( $\mu$ ) and between conical surfaces ( $\mu'$ ) are selected to range from 0 to 0.6. In addition, three conical slopes ( $\theta$ ) ranging from

10, 20 and 30 degrees are selected. Figure 4.5 shows the trends of the sliding force as the friction coefficients and conical slopes increases. In general, as the conical slope increases and as the friction coefficient increases, the SCFD becomes more efficient, where the ( $P_0$ ) can be achieved using smaller pretension forces in the PT tendons. By comparing the influence of the friction coefficients, the result shows the increase of the friction coefficient on the conical surfaces ( $\mu'$ ) has higher influence than increase the friction coefficient between flat plates ( $\mu$ ). Figure 4.6 shows the trends of the post yield stiffness as the friction coefficients and conical slopes increases. The trend for the post yield stiffness is like the trend observed in the sliding force presented above. Figure 4.7 shows the trends of the unloading stiffness as the friction coefficients and conical slopes increases. As shown in the figure, the unloading stiffness changes from positive to negative. The line where the unloading stiffness equals to zero represents the condition where the defined conical slopes equals to the critical angle. In general, as the friction coefficients and conical slopes increases, the absolute value of the unloading stiffness increases. Similarly, the result shows friction coefficient on the conical surfaces ( $\mu'$ ) has higher influence on the post yield stiffness than increase the friction coefficient between flat plates ( $\mu$ ).

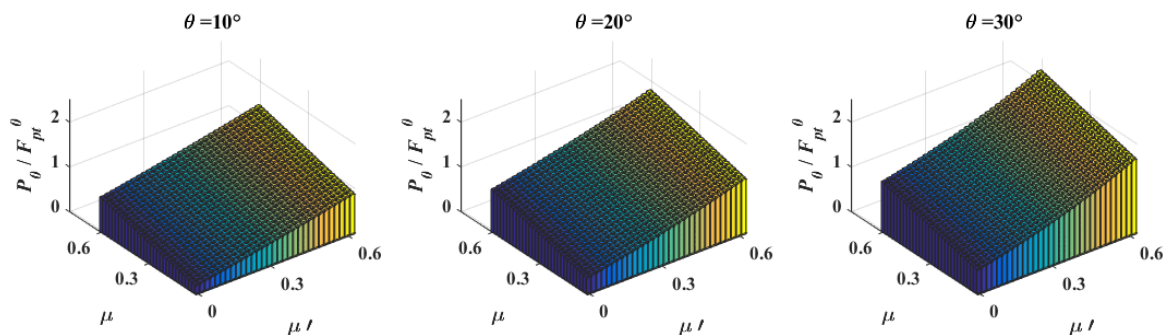


Figure 4.5 Normalized sliding force

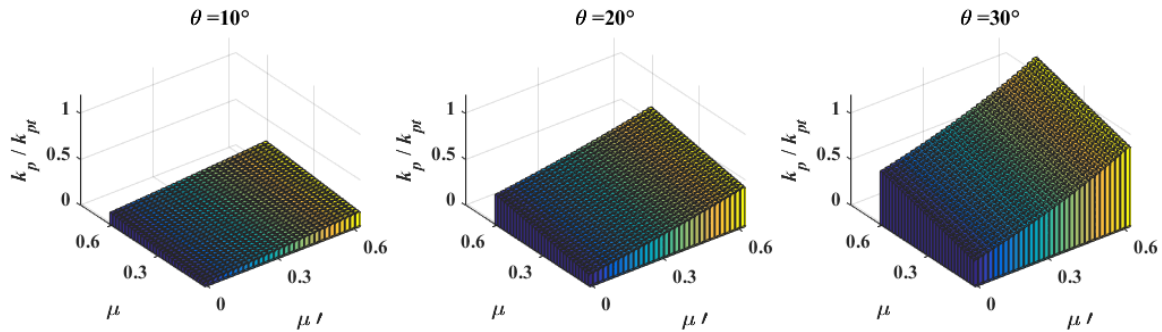


Figure 4.6 Normalized post stiffness

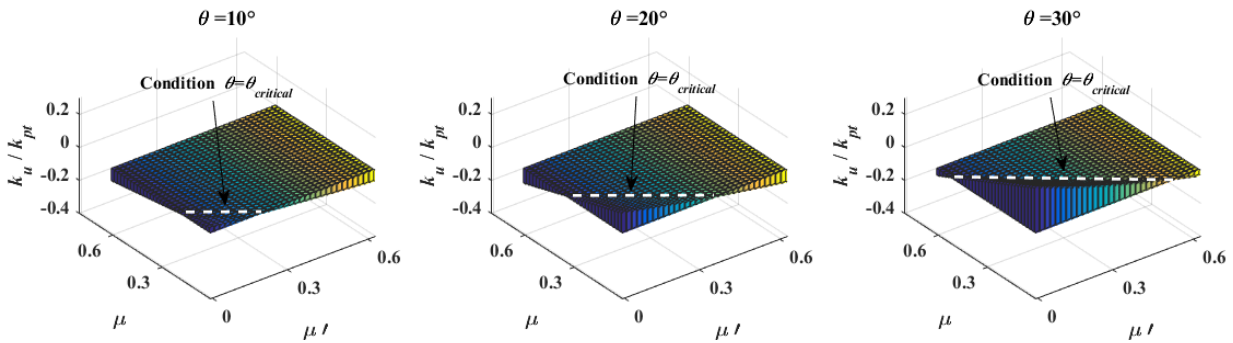


Figure 4.7 Normalized unloading stiffness

### 4.3 Optimal Design Approach

There are multiple ways to design the SCFD to achieve different force-deformation responses. Figure 4.8 shows the flow chart to design the SCFD using the minimum PT tension force and PT stiffness. As shown in Figure 4.5 to 4.7, as the friction coefficients ( $\mu$  and  $\mu'$ ) increases, the ratio of the  $P_0$ ,  $k_p$  and  $k_u$  over  $F_{pt}^0$  and  $k_{pt}$  increases. In addition, increase of  $\mu'$  might be more effective than increase of  $\mu$ . Hence, it is recommended that the designer started the design of with the maximum  $\mu'$  based on the available friction surfaces. Once  $\mu'$  is defined, the maximum slope

angle ( $\theta$ ) is defined using Equation 7. With  $\mu'$  and  $\theta$  defined, the critical  $\mu$  can be calculated using Equation 23.

$$\mu_{critical} = \frac{\tan\theta - \mu'}{1 + \mu' \cdot \tan\theta} \quad (23)$$

If  $\mu$  is less than  $\mu_{critical}$ , the hysteresis will be Type I (Figure 2.5). Similarly, if  $\mu$  is equal or greater than  $\mu_{critical}$ , the hysteresis will be Type II (Figure 2.5) and Type III (Figure 2.5), respectively. Designer can choose any value of  $\mu$  to achieve the same  $P_0$  and  $k_p$ . Finally, once the friction coefficient,  $\mu$  and  $\mu'$  and the slope angle ( $\theta$ ) are defined, the required PT stiffness and PT initial force can be calculated using Equation 10 and Equation 12.

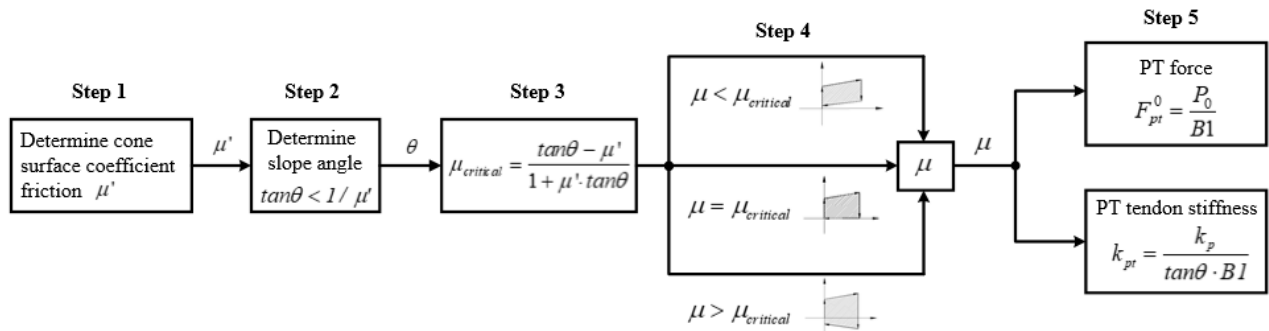


Figure 4.8 Flow chart of recommended design approach

For example, a sliding force of 100 kN and a post stiffness of 3kN/mm are required by the system design. Then the conical surfaces are manufactured to have a friction coefficient  $\mu'$  equal to 0.4 and a slope of 30 degree. It should be noted that the higher the conical slope is designed to be, the more opening the clamping plate will have as the same amount of deformation happens, which brings more demand for the deformation capacity of the washers. Equation 22 gives the corresponding critical friction coefficient  $\mu$  as 0.18. Assume hysteresis type II is the desired one,

the required pretension force and washer stiffness can be easily calculated as 69 kN and 3.6 kN/mm. To be noted, the pretension force can be evenly distributed to all the bolts so that the demand for each bolt is brought down. The demand for individual washer can also be customized by using different ways of stack.

#### **4.4 Summary**

This Chapter first presented the experimental results, which gives all sliding force and post tension stiffness obtained from the test. In addition, nine different tested hysteresis were summarized, and it was concluded that stiffness is independent on post tension force and sliding force is independent on PT tendon stiffness. Furthermore, energy dissipation plots showed good energy dissipation capability. Mechanism was also verified by the experimental results. Then parameter study was carried out, showing that larger slope angle and bigger friction coefficients can lead to less demand on required PT tendon stiffness and pretension force. In the end, a recommended design approach was proposed for designers to design the desired device in the future.

## Chapter 5: Summary and Conclusions

### 5.1 Conclusion

A novel self-centering friction damper was proposed and tested. By adopting conical surfaces in the design, SCFD can not only provide self-centering feature but also achieve bi-directional movements. Besides the conical surface, there is also a flat surface working together to have better capacity of energy dissipation. The use of two stoppers successfully balance the clamping plate and guide its motion as it opens and closes. It was designed to connect the structure through bolt connections, which takes much less time to construct and repair. A set of design equations were developed to calculate required conical slope, pretension force of high strength bolts and the corresponding post stiffness based on designed sliding force. In addition, prototype specimen was designed, fabricated and tested in the component experimental testing. It can be seen from the test results that the hysteretic responses were stable and well predicted in terms of theoretical calculations. Further parameter studies were carried out using the experimental results and verified equations. It was shown that characteristics of the entire hysteresis can be changed by different design parameters: friction coefficients, conical slopes, pretension force and effective stiffness of washers in stack:

1. Sliding force doesn't depend on the number of washers; the post stiffness doesn't depend on the pretension force.
2. Both post stiffness and unloading stiffness increases as the conical slope increases.
3. The required minimum conical slope to have self-centering mechanism becomes larger as there is more friction between either conical surfaces or flat surfaces.

4. More friction and higher conical slope can bring down the demand for pretension force and washer stiffness to reach the same magnitude of sliding force and post stiffness.
5. When it comes to energy dissipation capacity, higher pretension force and larger post stiffness can significantly increase the energy dissipation capacity. In addition, as the pretension force becomes higher and higher, post stiffness makes less difference to the energy dissipation.

Furthermore, an optimal design approach was proposed for future users. Using this design approach, users can easily obtain the required washer stiffness and bolt pretension force.

## **5.2 Future work**

This study mainly focuses on the new concept proposal, development of theoretical equations, simple test on two parameters and further parametric study. There is more work worth to carry out in the future research:

- More experimental tests are in need for trying more different friction pads and investigating how loading rate can change the hysteresis.
- Further research is necessary to optimize the damper design. The prototype in this study is a very initial version. Many bolt connections were adopted in this study. Easier and faster fabrication is important to lower the cost.
- This study only focuses on the component level. No system level study was carried out. Structural responses from system-level numerical and experimental studies can be used to evaluate its performance in structures subjected to earthquake. Therefore, more studies are required on structural analysis.

## Bibliography

- Aiken, I. D., Nims, D. K., Whittaker, A. S., & Kelly, J. M. (1993). Testing of Passive Energy Dissipation Systems. *Earthquake Spectra*, 9(3).
- Alehashem, S. M. S., Keyhani, A., & Pourmohammad, H. (2008). Behavior and performance of structures equipped with ADAS & TADAS dampers (a comparison with conventional structures). *The 14th World Conference on Earthquake Engineering*, 12–17.
- Amjadian, M., & Agrawal, A. K. (2017). A passive electromagnetic eddy current friction damper (PEMECFD): Theoretical and analytical modeling. *Structural Control and Health Monitoring*, 24(10). <https://doi.org/10.1002/stc.1978>
- ATC-24: Guidelines for Cyclic Seismic Testing of Components of Steel Structures. (1992). *Redwood City, Report Prepared for the Applied Technology Council*.
- Banjuradja, W. (2018). *Experimental and numerical studies on the nonlinear responses of welded wide flange fuses*. University of British Columbia.
- Barrett, R. T. (1990). Fastener design manual. *NASA Reference Publication*, 1228.
- Chan, R. W. K., & Albermani, F. (2008). Experimental study of steel slit damper for passive energy dissipation. *Engineering Structures*, 30(4), 1058–1066.  
<https://doi.org/10.1016/j.engstruct.2007.07.005>
- Christopoulos, C., & Montgomery, M. (2013). Viscoelastic coupling dampers (VCDs) for enhanced wind and seismic performance of high-rise buildings. *Earthquake Engineering and Structural Dynamics*, 42(15), 2217–2233. <https://doi.org/10.1002/eqe.2321>
- Filiatrault, A., Tremblay, R., & Kar, R. (2000). Performance evaluation of friction spring seismic damper. *Journal of Structural Engineering New York, N.Y.*, 126(4), 491–499.  
[https://doi.org/10.1061/\(ASCE\)0733-9445\(2000\)126:4\(491\)](https://doi.org/10.1061/(ASCE)0733-9445(2000)126:4(491))

- Gong, S., & Zhou, Y. (2017). Experimental study and numerical simulation on a new type of viscoelastic damper with strong nonlinear characteristics. *Structural Control and Health Monitoring*. <https://doi.org/10.1002/stc.1897>
- Grigorian, C. E., Yang, T. S., & Popov, E. P. (1993). Slotted Bolted Connection Energy Dissipators. *Earthquake Spectra*, 9(3), 491–504. <https://doi.org/10.1193/1.1585726>
- Hashemi, A., Zarnani, P., Masoudnia, R., & Quenneville, P. (2017). Seismic resistant rocking coupled walls with innovative Resilient Slip Friction (RSF) joints. *Journal of Constructional Steel Research*, 129, 215–226. <https://doi.org/10.1016/j.jcsr.2016.11.016>
- Kobori, T., Miura, Y., Fukusawa, E., Yamada, T., Arita, T., Takenake, Y., ... Fukumoto, T. (1992). Development and application of hysteresis steel dampers. *Proceedings of 11th World Conference on Earthquake Engineering*, 2341–2346.
- Li, T. (2018). *Experimental testing and numerical modelling of honeycomb structural fuse*. University of British Columbia.
- Ma, X., Borchers, E., Pena, A., Krawinkler, H., Billington, S., & Deierlein, G. G. (2010). Design and Behavior of Steel Shear Plates with Openings as Energy-Dissipating Fuses. *Internal Report, John A. Blume Earthquake Engineering Center, Stanford University*, (17).
- Mahjoubi, S., & Maleki, S. (2015). Seismic performance assessment of steel frames equipped with a novel passive damper using a new damper performance index. *Structural Control and Health Monitoring*, 22(4), 774–797. <https://doi.org/10.1002/stc.1717>
- Monir, H. S., & Zeynali, K. (2013). A modified friction damper for diagonal bracing of structures. *Journal of Constructional Steel Research*, 87, 17–30. <https://doi.org/10.1016/j.jcsr.2013.04.004>
- Montgomery, M., & Christopoulos, C. (2015). Experimental validation of viscoelastic coupling

- dampers for enhanced dynamic performance of high-rise buildings. *Journal of Structural Engineering (United States)*, 141(5). [https://doi.org/10.1061/\(ASCE\)ST.1943-541X.0001092](https://doi.org/10.1061/(ASCE)ST.1943-541X.0001092)
- Mualla, I. H., & Belev, B. (2002). Performance of steel frames with a new friction damper device under earthquake excitation. *Engineering Structures*, 24(3), 365–371. [https://doi.org/10.1016/S0141-0296\(01\)00102-X](https://doi.org/10.1016/S0141-0296(01)00102-X)
- Nims, D. K., Richter, P. J., & Bachman, R. E. (1993). The use of the energy dissipating restraint for seismic hazard mitigation. *Earthquake Spectra*, 9(3), 467–489. <https://doi.org/10.1193/1.1585725>
- Pall, A. S., & Marsh, C. (1982). RESPONSE OF FRICTION DAMPED BRACED FRAMES. *ASCE J Struct Div*, 108(ST6), 1313–1323.
- Reinhorn, A. M., Li, C., & Constantinou, M. C. (1995). Experimental and analytical investigation of seismic retrofit of structures with supplemental damping; Part 1, Fluid viscous damping devices. In *Technical Report - National Center for Earthquake Engineering Research*.
- Richter, P. J., Nims, D. K., Kelly, J. M., & Kallembach, R. M. (1990). The EDR-energy dissipating restraint. A new device for mitigation of seismic effects. *Proceedings of the 1990 SEAOC Convention*, 1, 377–401.
- Rojas, P., Ricles, J. M., & Sause, R. (2005). Seismic performance of post-tensioned steel moment resisting frames with friction devices. *Journal of Structural Engineering*, 131(4), 529–540. [https://doi.org/10.1061/\(ASCE\)0733-9445\(2005\)131:4\(529\)](https://doi.org/10.1061/(ASCE)0733-9445(2005)131:4(529))
- Soong, T. T., & Spencer, B. F. (2002). Supplemental energy dissipation: State-of-the-art and state-of-the-practice. *Engineering Structures*, 24(3), 243–259.

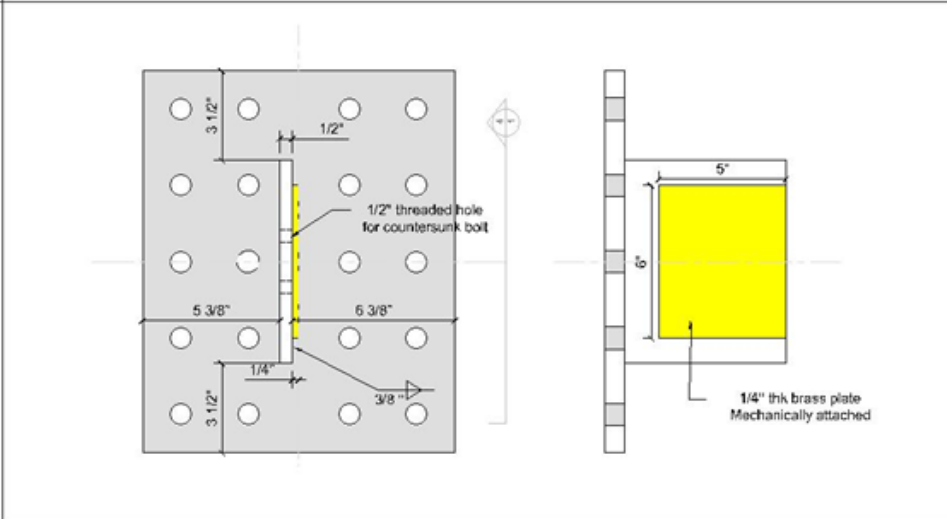
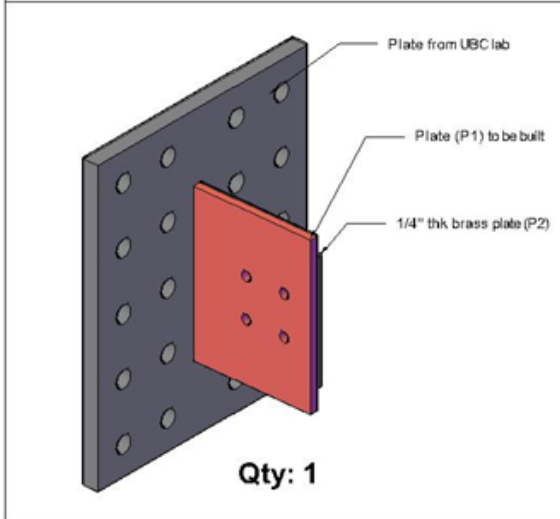
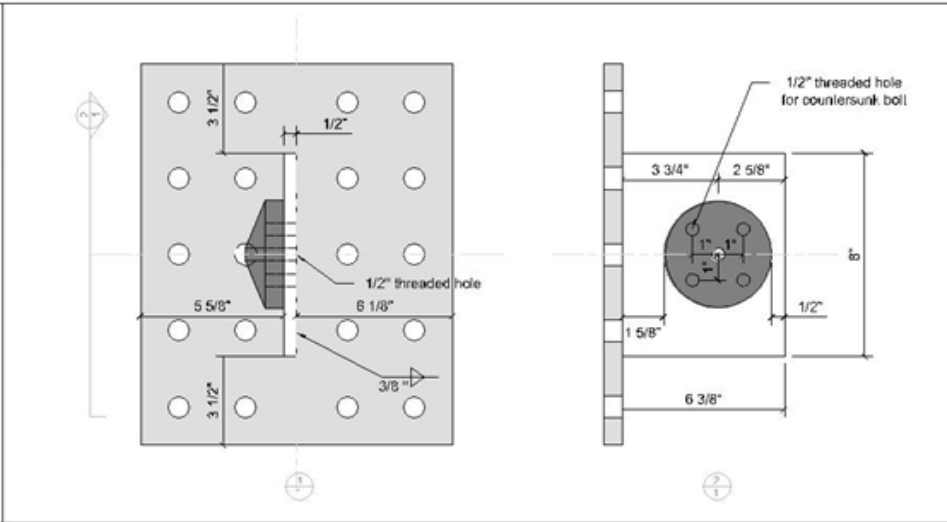
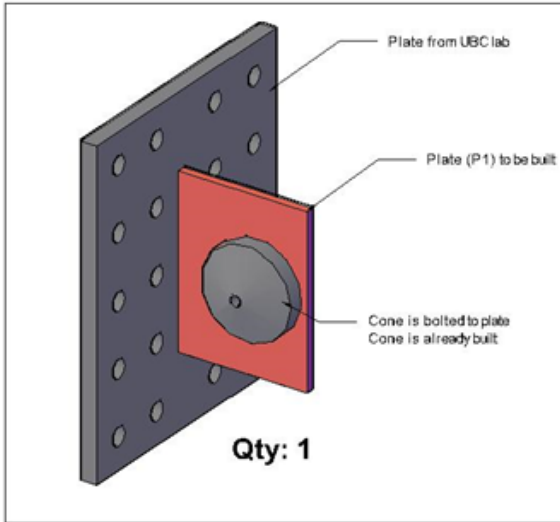
[https://doi.org/10.1016/S0141-0296\(01\)00092-X](https://doi.org/10.1016/S0141-0296(01)00092-X)

- Symans, M. D., Charney, F. A., Whittaker, A. S., Constantinou, M. C., Kircher, C. A., Johnson, M. W., & McNamara, R. J. (2008). Energy dissipation systems for seismic applications: Current practice and recent developments. *Journal of Structural Engineering*, *134*(1), 3–21. [https://doi.org/10.1061/\(ASCE\)0733-9445\(2008\)134:1\(3\)](https://doi.org/10.1061/(ASCE)0733-9445(2008)134:1(3))
- Tsai, K. C., Chou, C. C., Lin, C. L., Chen, P. C., & Jhang, S. J. (2008). Seismic self-centering steel beam-to-column moment connections using bolted friction devices. *Earthquake Engineering and Structural Dynamics*, *37*(4), 627–645. <https://doi.org/10.1002/eqe.779>
- Whittaker, A. S., Bertero, V. V., G., J. L. A., & Thompson, C. (1989). *Earthquake simulator testing of steel plate added damping and stiffness elements* (Vol. 89). Earthquake Engineering Research Center, University of California at Berkeley.
- Yang, T. Y., Li, T., Tobber, L., & Pan, X. (2019). Experimental and numerical study of honeycomb structural fuses. *Engineering Structures*, 109814.

## **Appendices**

### **Appendix A**

AutoCAD drawings for specimen fabrication:






THE UNIVERSITY OF BRITISH COLUMBIA  
**Smart Structures**

---

LEE-SEEF COLLABORATIVE SLAKE-TABLE TEST  
 NEX-GENERATOR EARTHQUAKE RESILIENT TALL BUILDING

**Detail - Component**

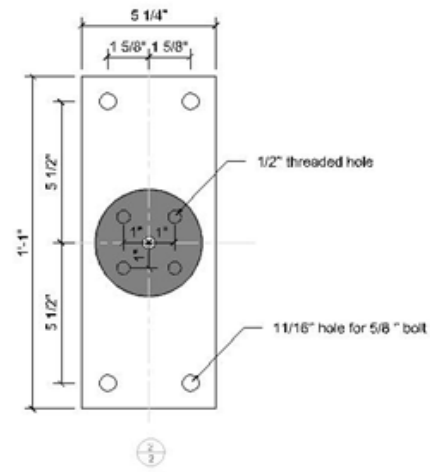
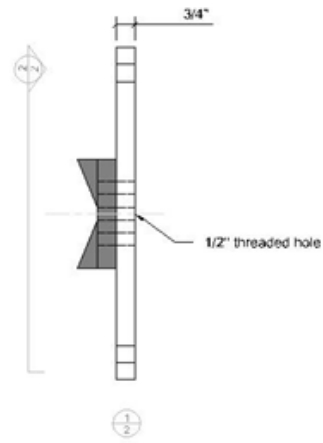
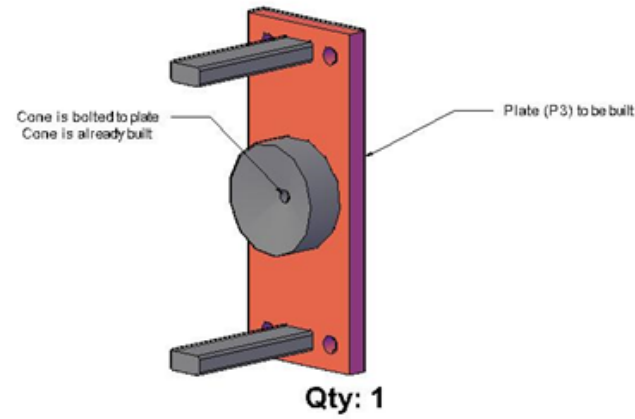
---

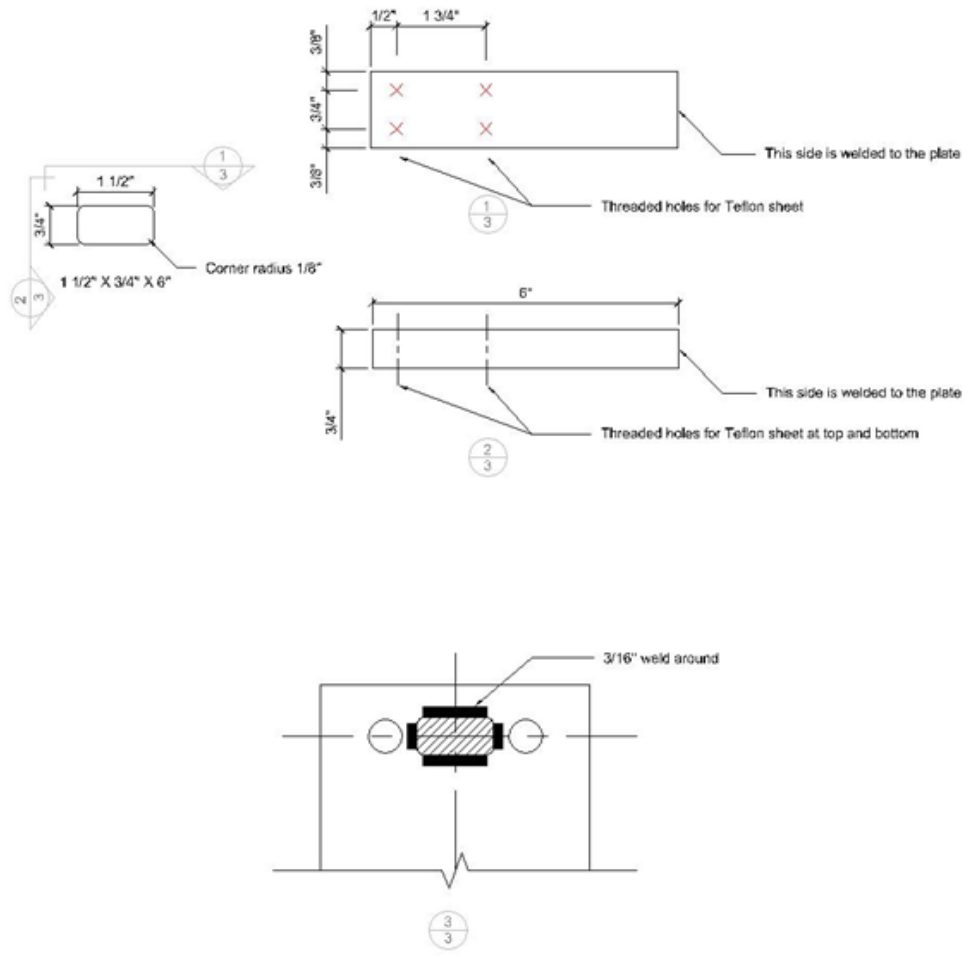
SHEET NO.  
**1**

DRAWN BY

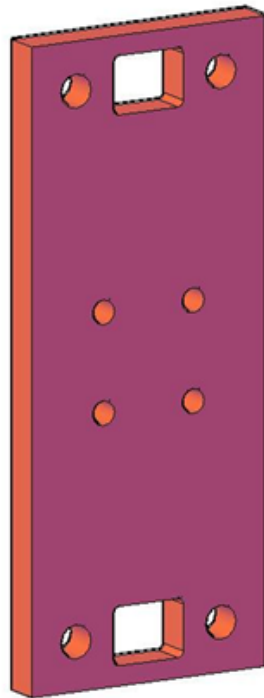
---

DATE 2018/11

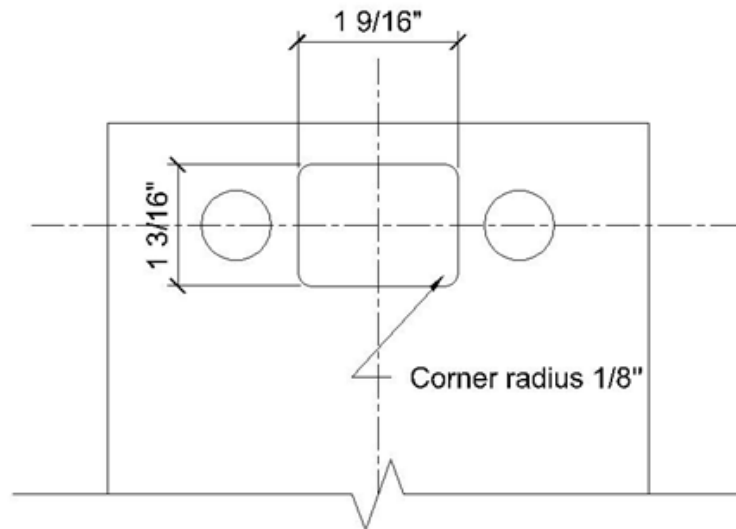


SHEET NO.	<b>3</b>
DRAWN BY	
DATE	2018/11



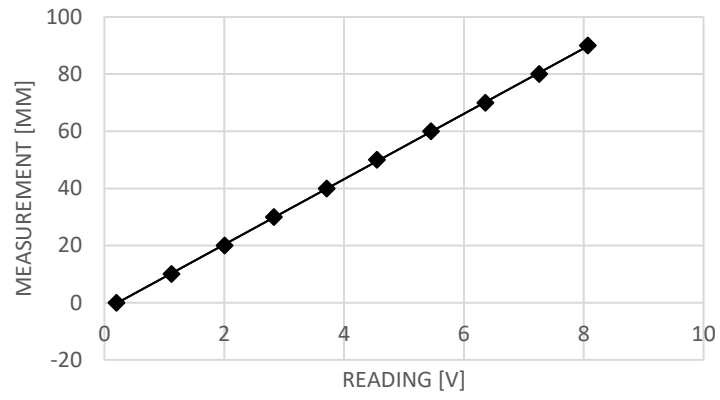
Qty: 1



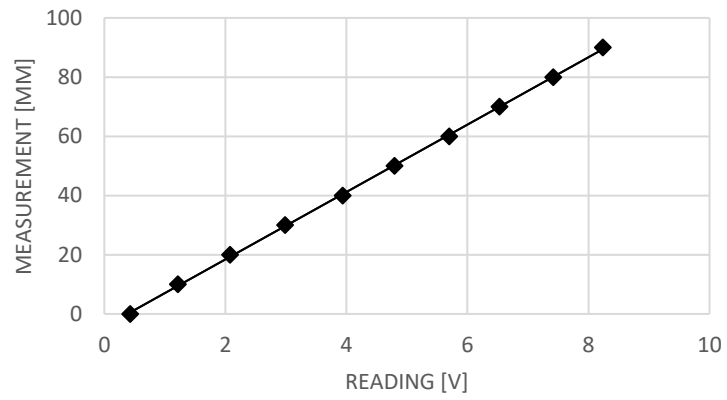
Other size follows drawing 2


## **Appendix B**

Calibration results of linear pots



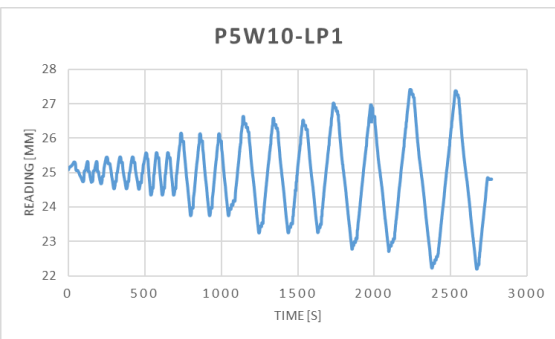
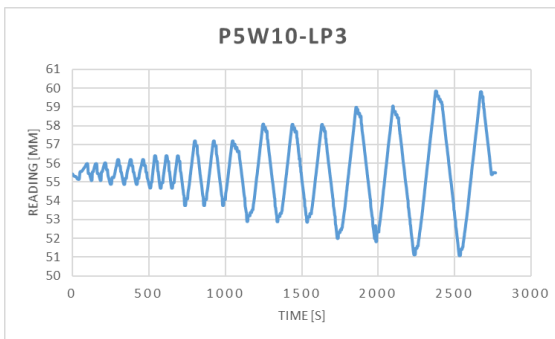
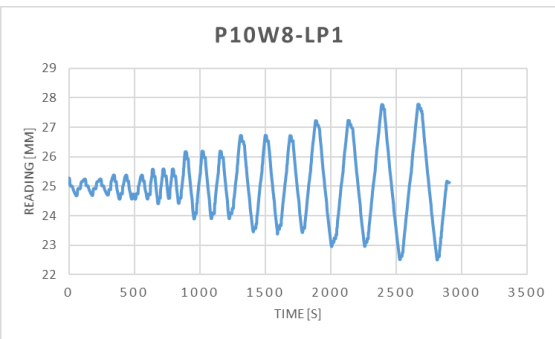
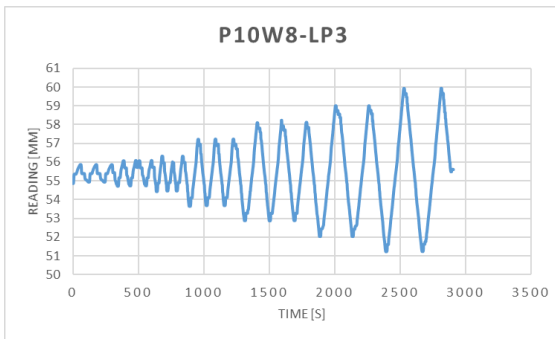
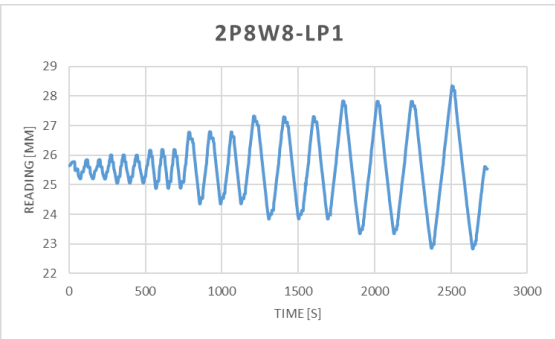
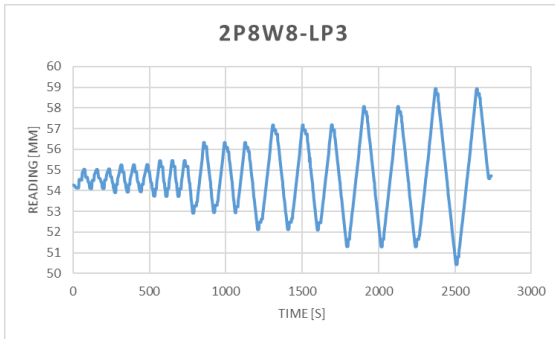
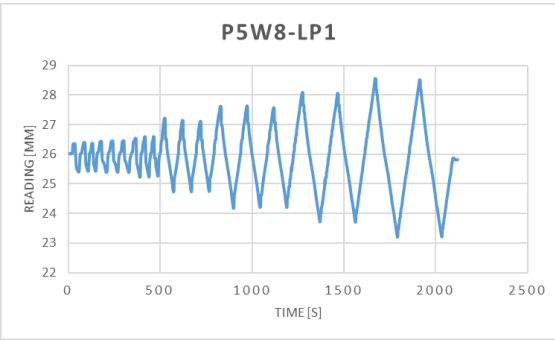
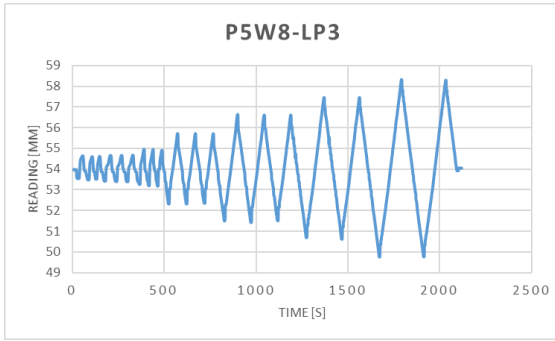
**LP3**

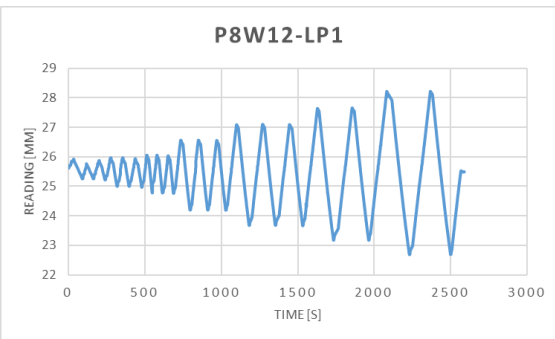
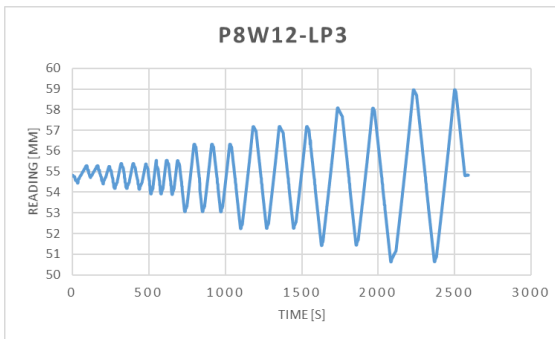
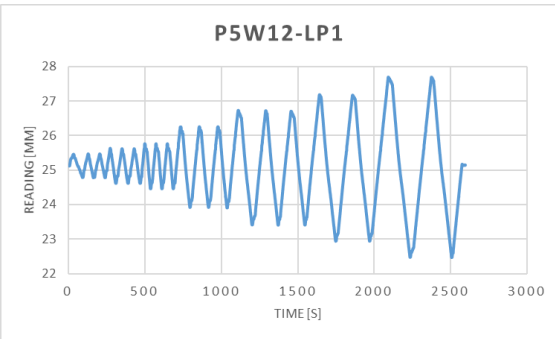
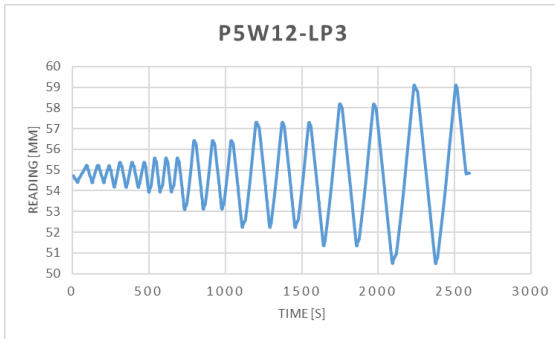
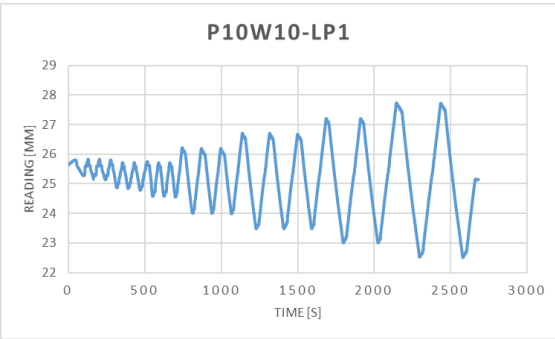
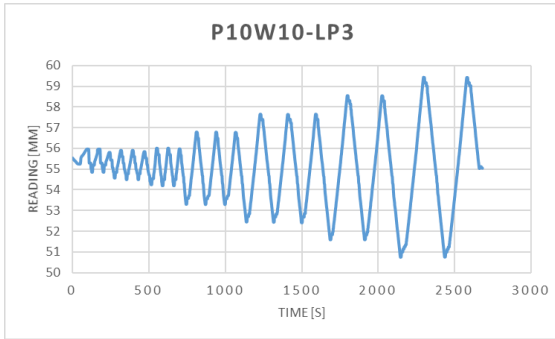
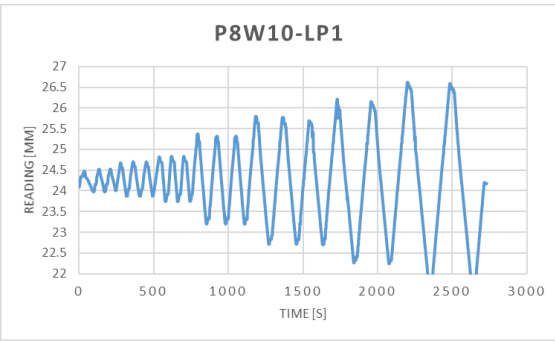
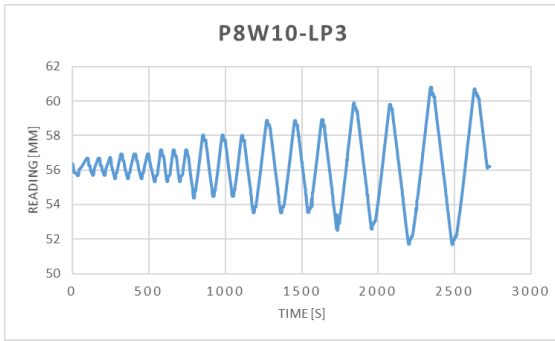


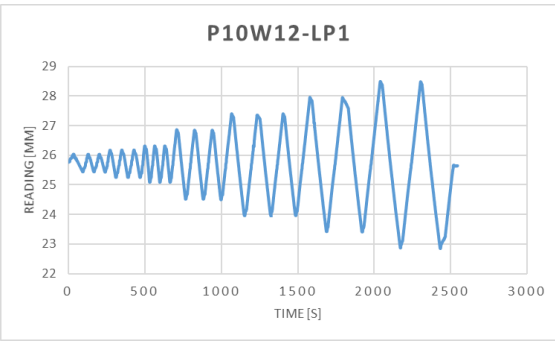
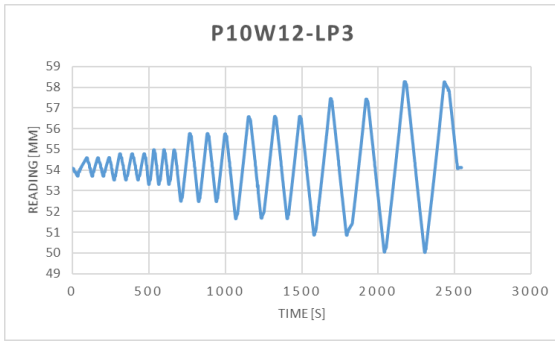
**LP1**

## **Appendix C**

Displacement records for two linear pots during each test:

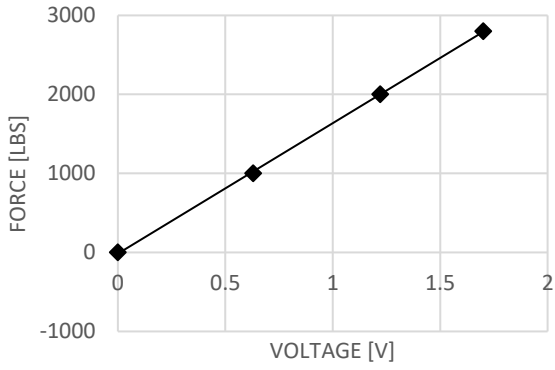




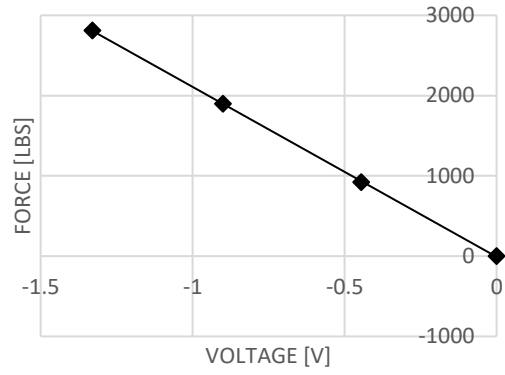


## **Appendix D**

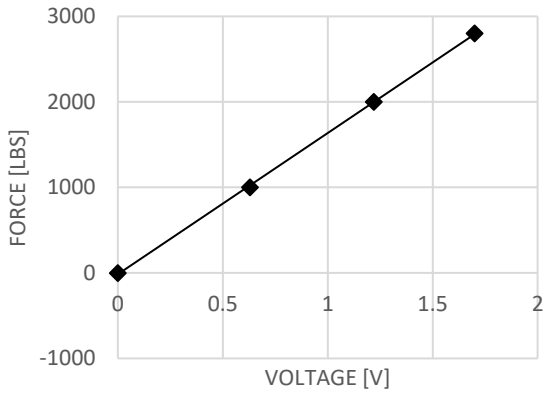
Calibration results in tensile test:



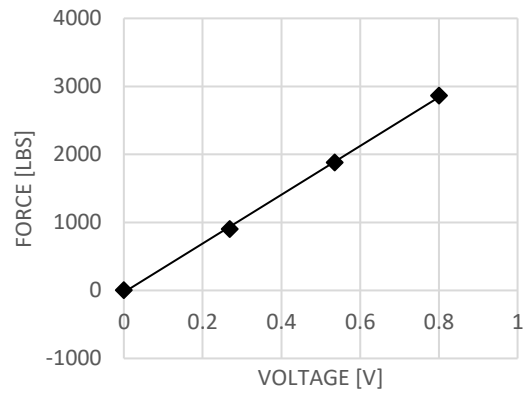
**SG0**



**SG1**



**SG2**



**SG3**

## **Appendix E**

Strain gauge records on the bolts:

